Molecular Cell

Article

Precise control of transcription condensates across S phase balances linker histone expression with DNA replication, ensuring genome stability

Graphical abstract

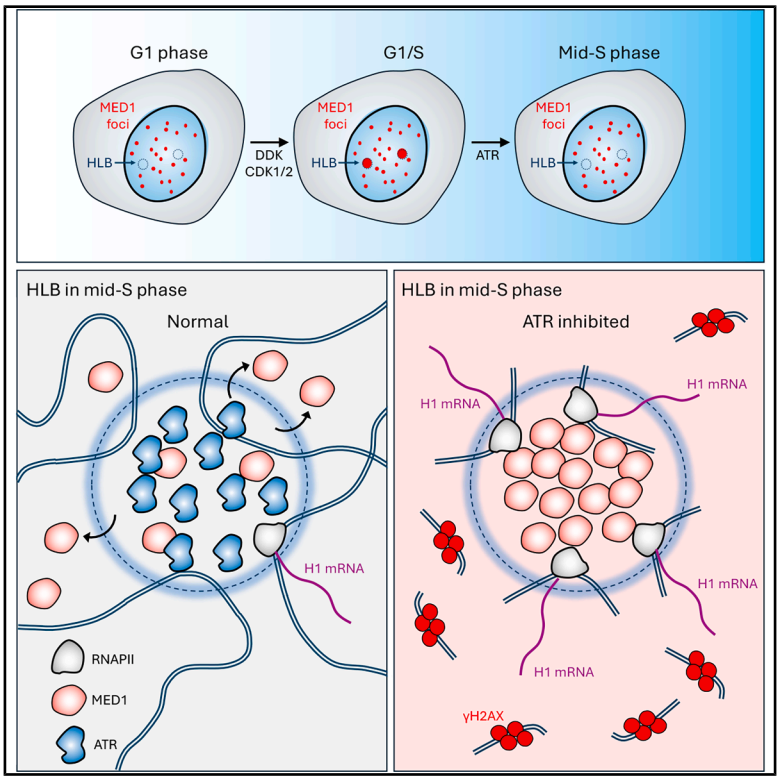

Highlights

- DDK and CDK1/2 induce transcription condensate formation at HLBs at the G1/S transition
- ATR is recruited to HLBs in mid-S phase and dissolves the transcription condensates
- ATR inhibition leads to linker histone H1.1 overexpression and subsequent DNA damage
- MED1^{IDR} boosts linker H1.1 expression and ATR inhibitor-induced DNA damage

Authors

Carlos Origel Marmolejo, Celina Sanchez, Erin Helms, ..., Paige Roberts, Stephan Hamperl, Joshua C. Saldivar

Correspondence

saldivaj@ohsu.edu

In brief

Marmolejo et al. uncover transcription condensate dynamics at histone locus bodies across the cell cycle. These dynamics are governed by cell cycle (DDK and CDK1/2) and checkpoint (ATR-CHK1) kinases to precisely control the "on/off" of histone gene transcription and maintain genome integrity.

Marmolejo et al., 2026, Molecular Cell *86*, 640–655
February 19, 2026
https://doi.org/10.1016/j.molcel.2026.01.005

CellPress

CellPress
OPEN ACCESS

Molecular Cell

Article

Precise control of transcription condensates across S phase balances linker histone expression with DNA replication, ensuring genome stability

Carlos Origel Marmolejo,[1,5] Celina Sanchez,[2] Erin Helms,[1] Melissa J. McEvoy,[2] Juyoung Lee,[1] Marcel Werner,[3] Paige Roberts,[1,6] Stephan Hamperl,[3] and Joshua C. Saldivar[1,4,7,*]

[1]Cancer Early Detection Advanced Research Center, Knight Cancer Institute, Oregon Health and Science University, Portland, OR, USA
[2]Program in Biomedical Sciences, School of Medicine, Oregon Health and Science University, Portland, OR, USA
[3]Institute of Epigenetics and Stem Cells, Helmholtz Munich, 81377 Munich, Germany
[4]Division of Oncological Sciences, Knight Cancer Institute, Oregon Health and Science University, Portland, OR, USA
[5]Present address: Recursion, Salt Lake City, UT, USA
[6]Present address: Providence Medical Center, Portland, OR, USA
[7]Lead contact
*Correspondence: saldivaj@ohsu.edu
https://doi.org/10.1016/j.molcel.2026.01.005

SUMMARY

Transcription condensates are liquid-like compartments where transcription factors, co-activators, and RNA polymerases are selectively enriched and regulate transcription initiation of associated genes. While the principles governing the enrichment of proteins within transcription condensates are being elucidated, mechanisms that coordinate condensate dynamics with other nuclear processes, such as DNA replication, have not been identified. We show in human cells that at the G1/S cell-cycle transition, large transcription condensates form at histone locus bodies (HLBs) in a cyclin-dependent kinase 1 and 2 (CDK1/2)-dependent manner. By mid-S phase, ataxia-telangiectasia and Rad3-related kinase (ATR) accumulates within HLBs and dissolves the associated condensates via its downstream effector, CHK1. Failure to dissolve condensates results in overexpression of linker H1 histones and nucleus-wide DNA damage. Moreover, an imbalance in the different linker histones accentuates DNA damage in ATR-CHK1-deficient cells. Our work reveals how transcription condensates are precisely controlled in the S phase to fine-tune gene activation and safeguard genome stability.

INTRODUCTION

The nucleus exhibits spatial organization through compartmentalization of chromatin regions where dynamic processes, such as transcription and replication, are active. These compartments lack membranes, yet they are enriched with proteins that are demixed from the nucleoplasm. In the case of transcription, compartmentalization can selectively raise the local concentration of functionally related proteins and exclude opposing factors, creating non-linear gene regulatory synergies.[1]

Models of transcription initiation suggest that in certain contexts it occurs in compartments referred to as transcription condensates.[2,3] These compartments exhibit liquid-like properties and are thought to influence the 3-dimensional architecture of chromatin, bringing enhancers and super-enhancers in proximity to promoters to drive gene expression.[4,5] Transcription condensates form through weak, multivalent protein-protein and protein-RNA interactions that stimulate liquid-liquid phase separation.[6] Their formation depends on various conditions (e.g., pH and co-solutes) and the concentrations of macromolecules within a solution.[1,7] Many transcription factors and co-activators, including MED1 (a subunit of the Mediator complex), contain intrinsically disordered regions (IDRs) that form multivalent interactions with other IDRs and RNA[8] and thereby undergo phase separation into condensates.

How these compartments are controlled with regard to their formation and dissolution is poorly understood. In proliferating cells, regulation of transcription condensate dynamics is particularly important as cells need to coordinate their spatial organization with DNA replication to maintain replication, transcription, and genome integrity.[9] Failure to coordinate transcription with replication can lead to conflicts and subsequent genome destabilization.[9]

In S phase, the most highly expressed genes are the replication-dependent histone genes, which encode both the nucleosomal core histones (H2A, H2B, H3, and H4) and the linker H1 histones (H1.1, H1.2, H1.3, H1.4, and H1.5).[10] These genes undergo a burst of expression at the G1/S transition in a

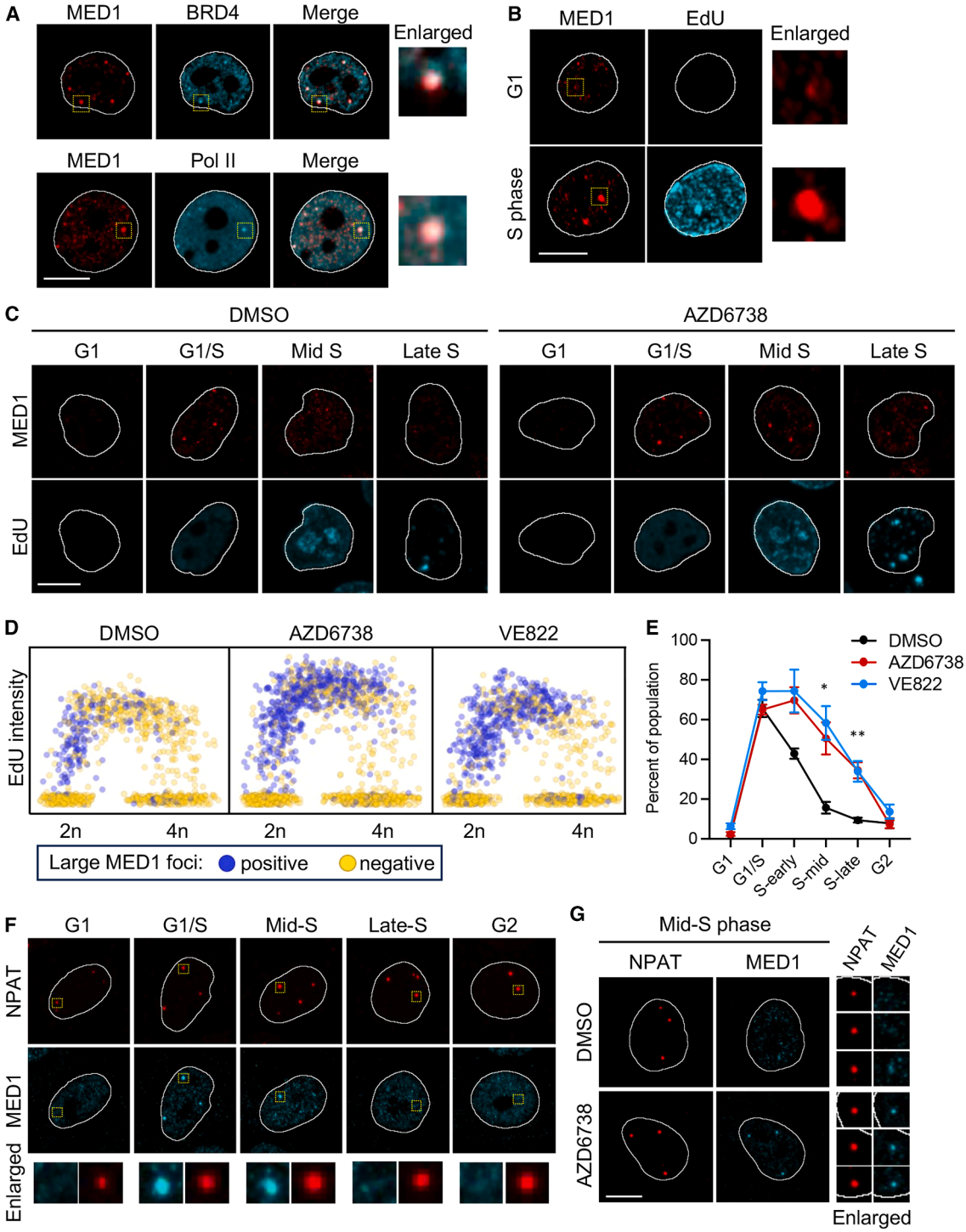

Figure 1. Large transcription condensates appear at the G1/S transition and are dissolved in mid-S phase by ATR kinase activity

(A) Representative images of MED1, BRD4, and RNAPII in MCF10A cells. Yellow boxes mark regions of enlarged condensates. Scale bar, 10 μm.

(B) Representative images of MED1 and EdU in MCF10A cells. Yellow boxes mark regions of enlarged condensates. Scale bar, 10 μm.

(C) Representative images of MED1 and EdU in MCF10A cells at various points in the cell cycle. Cell cycle phase was determined by QIBC as described in Figure S1C. Cells were treated with DMSO (mock) or 5 μM AZD6738 (ATR inhibitor) for 1 h. Scale bar, 10 μm.

(D) Scatterplot of DAPI integrated intensity (linear scale) and EdU mean intensity (log_2 scale) in MCF10A cells treated with DMSO (mock), 5 μM AZD6738 (ATR inhibitor), or 5 μM VE822 (ATR inhibitor) for 1 h. *2n* and 4n denote the DNA content. Cells positive for large MED1 foci (diameter > 0.7 μm) were colored purple, and negative cells were yellow.

(legend continued on next page)

cyclin-dependent kinase 2 (CDK2)-dependent manner.[11] Expression of the histone genes is coupled to S phase to ensure nucleosome content increases with DNA duplication.[12] The mechanisms that couple histone expression to S phase are only partially understood, and specifically, how and when cells downregulate histone expression are unknown.

Here, we uncover the mechanism that ensures precise control over histone expression, governed largely by the ATR pathway. We show ATR locally suppresses CDK2 and CDK1 activity to control transcription condensate dynamics, ensuring genome stability.

RESULTS

Transcription condensates form at the G1/S transition and are dissolved by ATR in mid-S phase

To investigate the regulation of transcription condensates across S phase, we imaged MED1 by indirect immunofluorescence confocal microscopy in MCF10A and RPE-1 hTERT cells. We labeled S phase cells using a 15-min EdU pulse prior to fixation. Consistent with previous reports,[2,13–15] MED1 formed foci throughout the nucleus. Notably, 10%–20% of cells contained 1–5 large MED1 foci (Figures S1A and S1B) that overlapped with RNA polymerase II (RNAPII) and BRD4 (Figure 1A), both known to be enriched within transcription condensates.[2,3] Intriguingly, the large MED1 foci were only present in EdU-positive cells (Figures 1B and S1A), suggesting a tight coupling to S phase.

ATR regulates transcription in S phase,[16] and thus we investigated the impact of ATR inhibition on the large transcription condensates. Within 1 h of ATR inhibition with AZD6738 or VE822, we observed a 2-fold increase in the percent of cells with large MED1 foci (Figure S1B). Given foci coupling to S phase, we integrated MED1 foci quantification across the cell cycle using quantitative image-based cytometry (QIBC)[17] (Figures S1C and S1D). Strikingly, the large foci appeared at the G1/S transition and disappeared in mid-S phase in an ATR-dependent manner (Figures 1C–1E and S1E), indicating ATR restricts foci to early S phase.

Next, we tested if MED1 foci were localized to DNA damage foci, given ATR's DNA damage response (DDR) functions.[18] However, the large MED1 foci did not colocalize with γH2AX or RPA32 (Figure S1F). Given the size and the number (1–5) of MED1 foci per cell, we reasoned the large condensates may instead form at nuclear bodies. The MED1 foci occasionally formed adjacent to Cajal bodies (Figure S1G), a spatial pattern that resembles the histone locus body (HLB).[19] HLBs are compartments that form around the replication-dependent histone genes and couple histone gene expression and RNA processing to S phase.[10,12,20] Indeed, co-staining NPAT, an HLB marker, revealed the large MED1 foci form at HLBs at the G1/S transition and then gradually dissolve during S phase progression (Figures 1F and 1G).

The abrupt appearance of MED1 at the HLB was dependent on CDC7, a DBF4-dependent kinase (DDK) that initiates replication origin firing (Figures S1H and S1I). In addition, we detected enrichment of DBF4 within HLBs (Figure S1J), suggesting CDC7-DBF4 couples the formation of transcription condensates at HLBs with the start of DNA synthesis.

ATR is recruited to HLBs in a transcription-dependent manner

Next, we examined ATR's subcellular localization relative to MED1 and NPAT. Co-staining with small interfering RNA (siRNA)-validated antibodies (Figure S2A) revealed a prominent co-localization of large ATR foci with the large MED1 foci and NPAT (Figures 2A and S2B). ATR levels increased in the HLBs during S phase and peaked by late-S phase (Figures 2B and 2C). We did not detect an enrichment of ATR activators ATRIP, TOPBP1, or ETAA1 within NPAT foci (Figure S2C), consistent with the lack of other DDR proteins γH2AX and RPA32 (Figure S1F).

At the start of S phase, histone genes within HLBs undergo a burst of transcription.[11] Given this, we asked whether ATR recruitment to HLBs was transcription dependent. A proximity ligation assay (PLA) revealed ATR and RNAPII can form PLA foci that are reduced by the transcription inhibitor, triptolide (Figure 2D). Triptolide also reduced ATR levels at HLBs (Figure 2C), indicating ATR recruitment to the compartment is transcription-dependent.

Next, we analyzed publicly available ATR CUT&RUN-seq and 4sU-seq data,[21] revealing ATR to be bound near the promoters of the most highly expressed genes (Figures 2E and S2D). Notably, ATR binding was even more enriched at the promoters of the 55 histone genes that make up the HIST1 cluster (Figure 2E). As the HIST1 cluster is ∼ 2 megabases (MB) long and histone genes contain a single exon, we compared ATR enrichment to other gene clusters of similar sizes or to other single-exon genes, and again, we observed a stronger enrichment of ATR at the HIST1 histone genes (Figure 2E). We conclude that transcription-dependent recruitment of ATR to histone gene promoters enriches ATR within HLBs, where it dissolves the associated transcription condensate in mid-to-late-S phase.

ATR signaling increases the sensitivity of S phase transcription condensates to dissolution by 1,6-hexanediol

Membrane-less compartments exist on a continuum across a liquid state, a gel-like state, and a solid state, depending in part on the properties of their macromolecular components.[1] In some contexts, liquid-like compartments can be differentiated from solid-like ones by 1,6-hexanediol (1,6-HXD),[22] though not

(E) Line plots showing the percent of MCF10A cells with large MED1 foci for each cell cycle phase. Cells were treated as in (D). Points and error bars are the mean and standard error, respectively, of 3 independent experiments. *$p < 0.05$, **$p < 0.01$.
(F) Representative images of MED1 and NPAT in MCF10A cells at various points in the cell cycle. Yellow boxes mark regions of enlarged condensates. Scale bar, 10 μm.
(G) Representative images of MED1 and NPAT in mid-S phase MCF10A cells. Cells were treated with DMSO (mock) or 5 μM AZD6738 (ATR inhibitor) for 1 h. Each NPAT-marked HLB focus was enlarged. Scale bar, 10 μm.

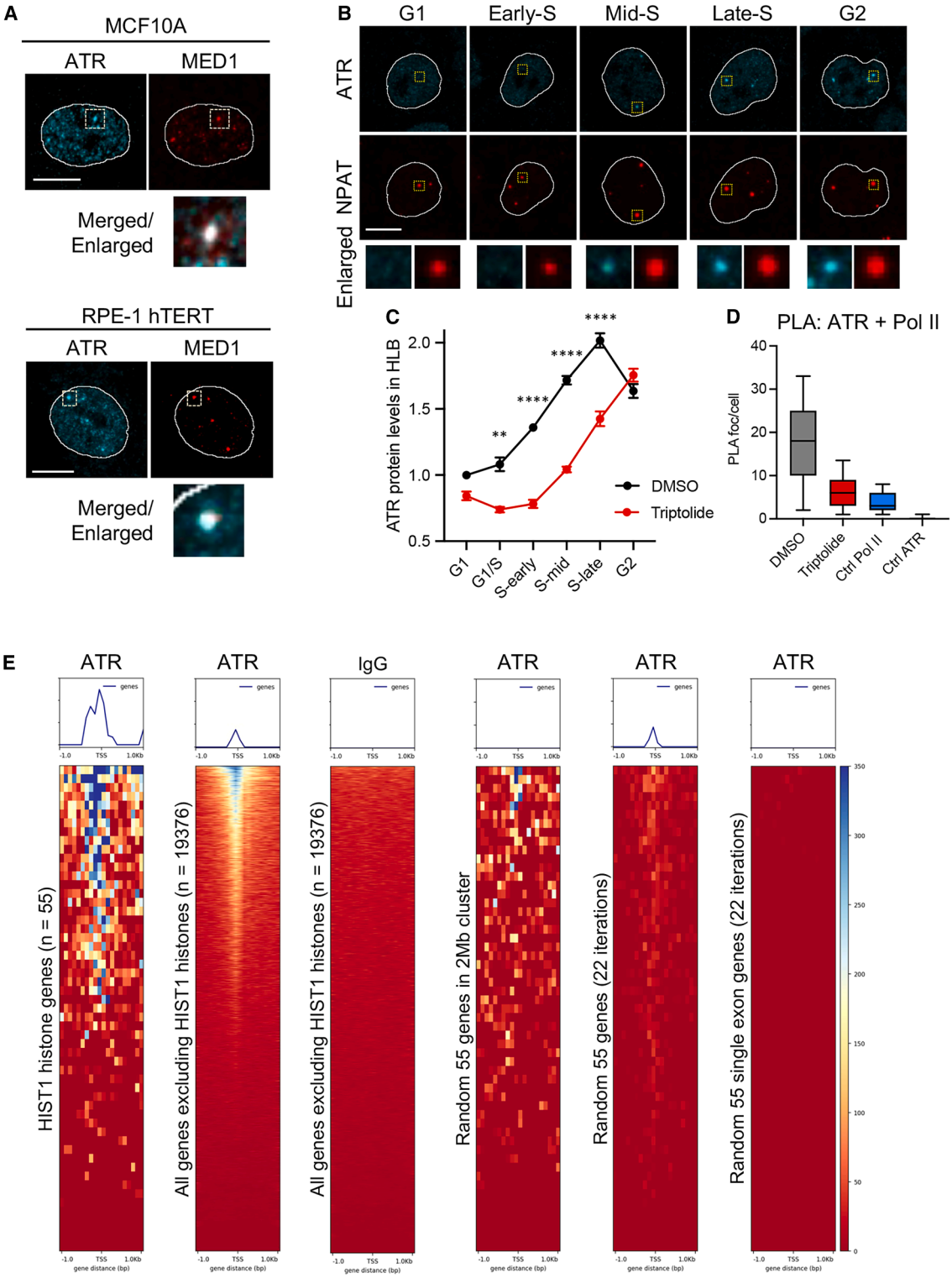

Figure 2. Transcription-dependent recruitment of ATR to S phase condensates at HLBs

(A) Representative images of MED1 and ATR in MCF10A (upper panels) and RPE-1 hTERT cells (lower panels). Yellow boxes mark regions of enlarged condensates. Scale bar, 10 μm.

(B) Representative images of ATR and NPAT in MCF10A cells at various points in the cell cycle. Yellow boxes mark regions of enlarged condensates. Scale bar, 10 μm.

(legend continued on next page)

all phase separations are affected by this aliphatic alcohol.[7] To investigate the biophysical properties of the large MED1 foci, we treated cells with 1,6-HXD for 1 min, a short exposure to minimize cellular malformations and nuclear artifacts.[22] Consistent with previous reports,[2,23] MED1 foci were disrupted within 1 min by increasing concentrations of 1,6-HXD (Figures 3A and 3B). Examination of the effect of 1,6-HXD on MED1 foci across the cell cycle revealed a striking impact on MED1 foci at HLBs in S phase (Figure 3C). Notably, the G1/S foci, and to a lesser degree the early S phase foci, were more resistant to disruption by 1,6-HXD compared with mid- and late-S phase foci (Figure 3D). Furthermore, in mid-S phase when the large MED1 foci dissolve in an ATR-dependent manner, we observed specifically these large foci (0.4–0.6 μm^2 area) to be the most sensitive to 1,6-HXD treatment (Figure 3E). These findings suggest the biophysical properties of MED1 foci at HLBs change during S phase progression, leading to their dissolution in mid-S phase.

Next, we tested the effect of 1,6-HXD on NPAT and ATR foci. Consistent with NPAT acting as a scaffold for the HLB, the NPAT foci were largely unaffected by treatment with 1,6-HXD except for at the highest concentration (Figures S3A–S3D). Curiously, 1,6-HXD increased the number of ATR foci throughout the cell cycle irrespective of focus size (Figures S3E–S3H). Thus, while NPAT and ATR are key components of the HLB, their enrichment in the compartment might not be driven by multivalent interactions involving IDRs like that of MED1. Accordingly, the HLB is a compartment that contains both structural components (NPAT), dynamic liquid-like components (MED1), and dynamic components with unknown features (ATR).

Given that mid-S phase condensates dissolve from HLBs in an ATR-dependent manner, we asked whether ATR influenced the biophysical properties of MED1. Strikingly, the large MED1 foci in mid-S phase became resistant to 1,6-HXD treatment after 1 h inhibition of ATR (Figures 3F and 3G). Resistance to 1,6-HXD was more prominent in cells that were further progressed in S phase, with the G1/S population largely unaffected by ATR inhibition and the late-S phase population most strongly affected (Figure 3H). We conclude that ATR kinase alters the biophysical properties of the transcription condensate components as cells progress through S phase, causing them to dissolve.

Cell-cycle checkpoint signaling controls S phase transcription condensate dynamics

To investigate the mechanism through which ATR controls MED1 dynamics across S phase, we asked whether CHK1, a downstream effector kinase of ATR that regulates the S phase cell-cycle checkpoint,[18] also controlled MED1 foci. Using two different CHK1 inhibitors (LY2603618 and ChIR-124), we found that, like ATR, CHK1 inhibition resulted in the persistence of MED1 foci at HLBs into late-S phase (Figures 4A and 4B).

ATR-CHK1 signaling during S phase limits the kinase activities of CDK1 and CDK2 (CDK1/2).[18,24,25] Accordingly, the persistence of MED1 foci into late-S phase may be caused by hyperactive CDK1 and/or CDK2. Indeed, CDK2 phosphorylates NPAT at the G1/S transition to promote the burst in histone expression,[11,26–28] suggesting CDK2 may be present in the HLB. Individual inhibition of either CDK1 or CDK2, with RO-3306 or NU6140, respectively, had little impact on MED1 foci (Figures S4A and S4B). By contrast, combined inhibition of CDK1/2 with BMS-265246 resulted in a near-complete loss of large MED1 foci in S phase, even in cells with ATR inhibition (Figures 4C–4E). The CDK1/2 inhibitor also reduced global transcription by ~20% as measured by EU labeling of nascent RNA (Figure 4F), implicating these cell-cycle CDKs as possibly having either direct or indirect transcription-specific roles.

CHK1 and CDK1/2 inhibitor data implicate HLBs as compartments where the ATR-CHK1 pathway suppresses CDK1/2 activity. In support of this, we observed phosphorylation of FOXM1 at T600 (pFOXM1), a CDK1/2-dependent event, to be focally enriched at HLBs (Figures 4G and 4H). FOXM1 is normally phosphorylated in the G2 phase but is prematurely phosphorylated by CDK1 in S phase when the ATR-enforced S/G2 checkpoint is inhibited,[16,29,30] and we observed this premature phosphorylation to also occur within HLBs (Figures 4G and 4H). Moreover, using PLA labeling, we found both CDK2 and CDK1 in close proximity to MED1, especially in S phase cells (Figures 4I, 4J, and S4C).

Given that ATR-CHK1 promotes the dissolution of HLB-specific transcription condensates, we predicted replication stress would prematurely dissolve MED1 foci in early S phase. Indeed, both hydroxyurea- and aphidicolin-induced replication stress caused a complete loss of the large MED1 foci within 1 h (Figure S4D). Collectively, the data show that ATR-CHK1 signaling dissolves S phase transcription condensates by suppressing CDK1/2 locally within HLBs.

Deregulation of HLB dynamics causes genome instability in ATR-CHK1-inhibited cells

ATR safeguards the integrity of the genome and is essential for cell viability,[31–34] and accordingly, we asked whether the essentiality of ATR is linked to its role in regulating MED1 at HLBs. Using a published CRISPR-Cas9 screen,[35] we averaged the normalized *Z* scores in three cell lines (MCF10A, HCT116, and HEK293) to identify genes that induce lethality upon ATR inhibition. Importantly, MED1 was among the top hits (Figure 5A). NPAT was on the opposite end from MED1 on the *Z* score plot, suggesting NPAT loss increases sensitivity to ATR inhibition. The opposing effects of NPAT and MED1 point to deregulation of HLB dynamics as a key driver of ATR inhibitor sensitivity.

ATR inhibitors induce pan-nuclear γH2AX, indicative of nucleus-wide DNA damage,[17,36] and we asked whether this

(C) Line plots showing the levels of ATR in NPAT-marked HLBs measured by immunofluorescence. MCF10A cells were treated with DMSO (mock) or 1 μM triptolide for 2 h. Points and error bars are the mean and standard error, respectively, of 3 independent experiments. $^{**}p < 0.01$ and $^{****}p < 0.0001$.
(D) Boxplots showing the quantification of PLA foci of ATR and RNAPII per cell. Cells were treated with mock (DMSO) or 1 μM triptolide for 2 h. Ctrl RNAPII and Ctrl ATR are single-antibody controls from cells treated with DMSO for 1 h.
(E) Metaplots and heatmaps showing ATR CUT&RUN reads center at the transcription start site (TSS) of different gene groups (all genes, histone-only genes, and random genes). Data are from Solvie et al.[21] and were publicly available.

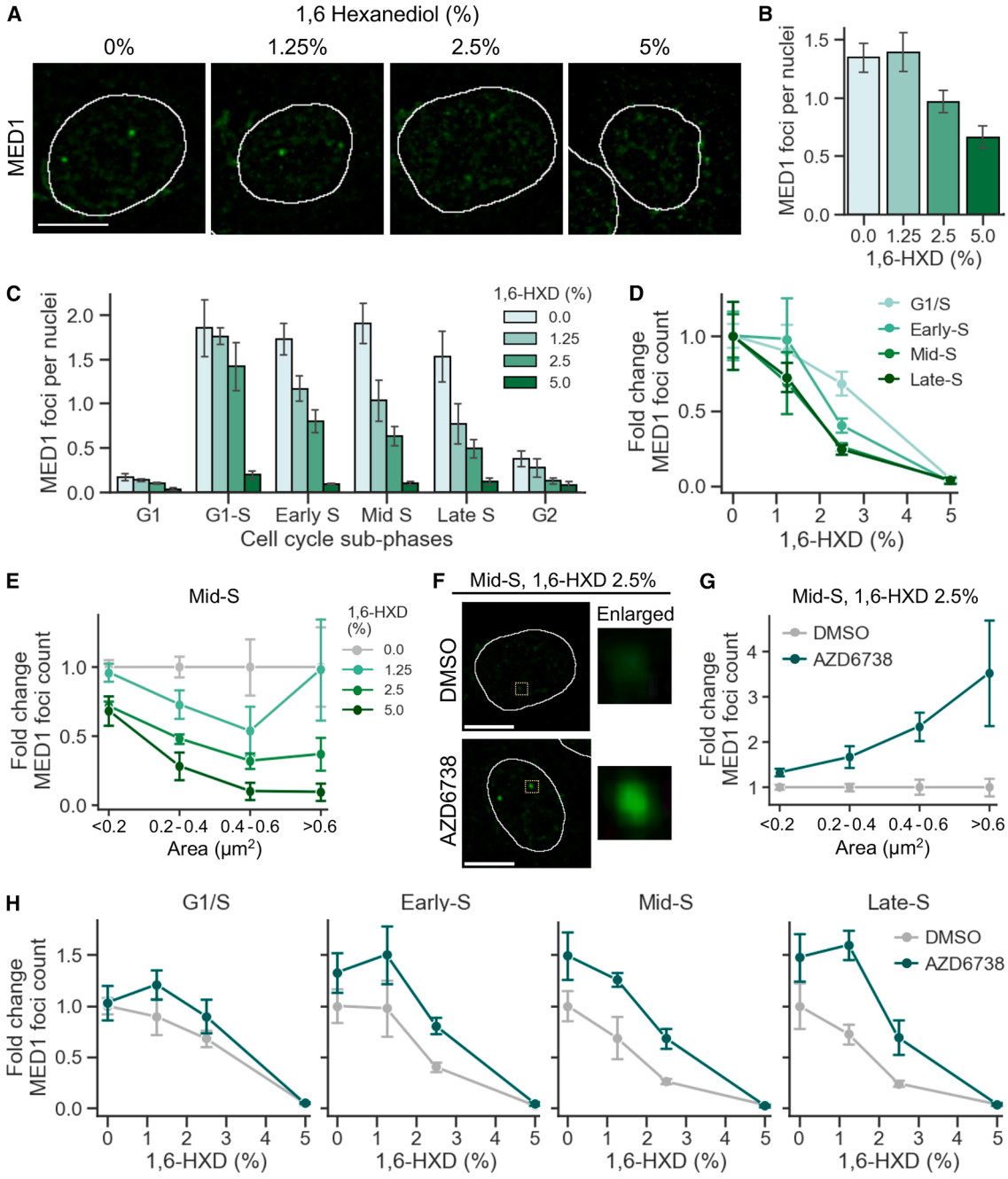

Figure 3. ATR increases the sensitivity of S phase transcription condensates to 1,6-hexanediol

(A) Representative images of MED1 in mid-S phase MCF10A cells. Cells were treated with 0%, 1.25%, 2.5%, or 5% 1,6-hexanediol (1,6-HXD) for 1 min. Scale bar, 10 μm.

(B) Bar plot showing the quantification of MED1 foci (diameter > 0.7 μm) in cells treated with varying concentrations (0%, 1.25%, 2.5%, and 5%) of 1,6-HXD for 1 min. Bars and error bars are the mean and standard error, respectively, of 3 independent experiments.

(C) Bar plot showing the quantification of MED1 foci (diameter > 0.7 μm) in cells treated with varying concentrations (0%, 1.25%, 2.5%, and 5%) of 1,6-HXD for 1 min at different stages of the cell cycle. The color of each bar corresponds to the concentration of 1,6-HXD used. Bars and error bars are the mean and standard error, respectively, of 3 independent experiments.

(D) Line plot showing the fold change in the number of MED1 foci following a 1 min treatment with 1.25%, 2.5%, or 5% 1,6-HXD compared with 0% 1,6-HXD. The fold change is calculated across G1/S, early-S, mid-S, and late-S phases. Each line represents a different cell cycle phase. Cells were treated as in (C). Points and error bars are the mean and standard error, respectively, of 3 independent experiments.

(legend continued on next page)

damage is due to deregulated HLBs. We inhibited ATR for 2–10 h and measured pan-nuclear γH2AX across the cell cycle. We observed a population of cells with an approximate 10-fold increase in γH2AX (γH2AX^{high}) that first appeared after 2 h of ATR inhibition (Figure S5A), was pan-nuclear, and coincided with early S phase (Figure 5B). Across the time course, cells with pan-nuclear DNA damage increased (Figure 5C) and moved toward G2 until exiting S phase with under-replicated DNA (Figures 5D and 5E).

Strikingly, MED1 knockdown (siMED1) (Figures S5B and S5C) caused a near-complete rescue of ATR and CHK1 inhibition-induced pan-nuclear DNA damage (Figures 5F and 5G). We observed mitotic slippage upon prolonged ATR or CHK1 inhibition (20 h) that was also rescued by MED1 knockdown, confirming MED1 as a driver of genome instability in ATR-CHK1-deficient cells (Figures 5H and 5I). MED1 knockdown only marginally decreased EdU incorporation (Figure S5D) and had no effect on EU incorporation (Figures S5E and S5F), suggesting the rescue of pan-nuclear DNA damage is not due to global loss of DNA replication or transcription.

Next, we knocked down 7 different mediator subunits (Figures S5G and S5H) and measured γH2AX in ATR and CHK1 inhibited cells. Of these, only MED12 and MED24 knockdown rescued the pan-nuclear DNA damage (Figure S5I). Importantly, MED12 and MED24 were also identified in the CRISPR screen as drivers of sensitivity to ATR inhibition (Figure S5G).[35] Knockdown of MED4, MED6, MED17, MED18, and MED26 had little to no impact on γH2AX (Figure S5J). Consistent with this finding, these subunits were not implicated as drivers of sensitivity to ATR inhibition (Figure S5G). These data suggest that ATR inhibition leads to MED1-induced lethality independently of a fully intact Mediator complex.

Finally, we tested the impact of NPAT knockdown (siNPAT), given that it had the opposite effect as MED1 in the published CRISPR screen[35] (Figure 5A). In contrast to MED1, loss of NPAT accelerated the formation of pan-nuclear DNA damage upon ATR or CHK1 inhibition (Figure 5J). Together, the data suggest that HLBs are central ATR-regulated compartments underlying the global DNA damage, chromosome instability, and loss of cell viability in ATR-inhibited cells.

MED1 does not induce replication catastrophe or excessive origin firing in ATR-inhibited cells

Next, we tested if MED1 knockdown could rescue replication catastrophe, a severe phenotype that occurs within 1–2 h when ATR inhibitors are combined with replication inhibitors (e.g., aphidicolin) and can be tracked by quantifying chromatin-bound RPA levels and γH2AX levels.[17] Once the RPA pool has been exhausted, replication forks are degraded throughout the nucleus. Intriguingly, MED1 knockdown did not prevent RPA exhaustion nor rescue γH2AX levels associated with replication catastrophe (Figures 5K and S5K).

Notably, ATR inhibition alone increased RPA levels on chromatin that was associated with pan-nuclear γH2AX (Figures 5L and S5K). Despite the observation that MED1 knockdown significantly reduced pan-nuclear γH2AX, RPA levels remained elevated (Figure 5L), effectively decoupling RPA accumulation on chromatin from DNA damage. Moreover, RPA exhaustion did not appear to be required for DNA damage induced by ATR inhibition, as many cells with high γH2AX levels were below the RPA threshold (Figure S5K). There was also a population of cells that had RPA levels exceeding the levels triggered by replication catastrophe (Figure S5K), raising the possibility that the pool of RPA does not fully exhaust in cells treated with aphidicolin and ATR inhibitors. These data suggest the DNA damage induced by MED1 in ATR-inhibited cells is not due to replication catastrophe associated with the exhaustion of RPA pools.

ATR prevents excessive origin firing by regulating the recruitment of CDC45 to licensed origins, a key step needed to activate the MCM replicative helicase.[18] Consistent with this role of ATR, we observed an approximate 3-fold increase in CDC45 recruitment to chromatin in S phase within 1 h of ATR inhibition, and knockdown of MED1 failed to rescue this hyper-loading of CDC45 (Figures S5L and S5M). Collectively, these data argue that MED1 does not induce replication catastrophe in ATR-inhibited cells. Instead, they reveal a clear distinction between ATR's function in response to chemically induced replication fork stalling and its functions in an unperturbed S phase, where it regulates MED1 at the HLB and prevents pan-nuclear DNA damage.

Linker H1 histone imbalance induces pan-nuclear DNA damage in ATR-inhibited cells

Next, we investigated how deregulation of MED1 induced DNA damage in ATR-inhibited cells. We hypothesized the increase in MED1 at the HLB upon ATR inhibition would alter the expression of histone genes, and this in turn would lead to nucleus-wide DNA damage. To test this hypothesis, we inhibited ATR for 2 h when the pan-nuclear γH2AX first appears (Figures 5D and S5A). Cells with pan-nuclear staining (γH2AX^{high}) consistently showed elevated linker histone H1 levels, with linker H1.1 most elevated (Figures 6A and 6B). The core histones were largely

(E) Line plot illustrating the fold change in the number of MED1 foci following a 1 min treatment with 1.25%, 2.5%, and 5% 1,6-HXD compared with 0% 1,6-HXD. The fold change is calculated across four distinct groups of MED1 foci categorized by area: <0.2, 0.2 to 0.4, 0.4 to 0.6, and >0.6 μm^2. Each line represents a different 1,6-HXD concentration. Points and error bars are the mean and standard error, respectively, of 3 independent experiments.

(F) Representative images of MED1 in mid-S phase cells treated with 2.5% 1,6-HXD for 1 min. Yellow boxes mark regions of enlarged condensates. Scale bar, 10 μm.

(G) Line plot showing the fold change in the number of MED1 foci in mid-S phase cells after a 1 h treatment with 5 μM AZD6738 compared with DMSO. Cells were also treated with 2.5% 1,6-HXD. The fold change is calculated across four distinct groups of MED1 foci categorized by area: <0.2, 0.2 to 0.4, 0.4 to 0.6, and >0.6 μm^2. Each line represents a different treatment condition (DMSO or AZD6738). Points and error bars are the mean and standard error, respectively, of 3 independent experiments.

(H) Line plot showing the fold change in the number of MED1 foci in cells treated with DMSO or 5 μM AZD6738 for 1 h, followed by a 1 min treatment with 1.25%, 2.5%, and 5% 1,6-HXD compared with 0% 1,6-HXD. The fold change is calculated across G1/S, early-S, mid-S, and late-S phases. Each line represents a different treatment condition (DMSO or AZD6738). Points and error bars are the mean and standard error, respectively, of 3 independent experiments.

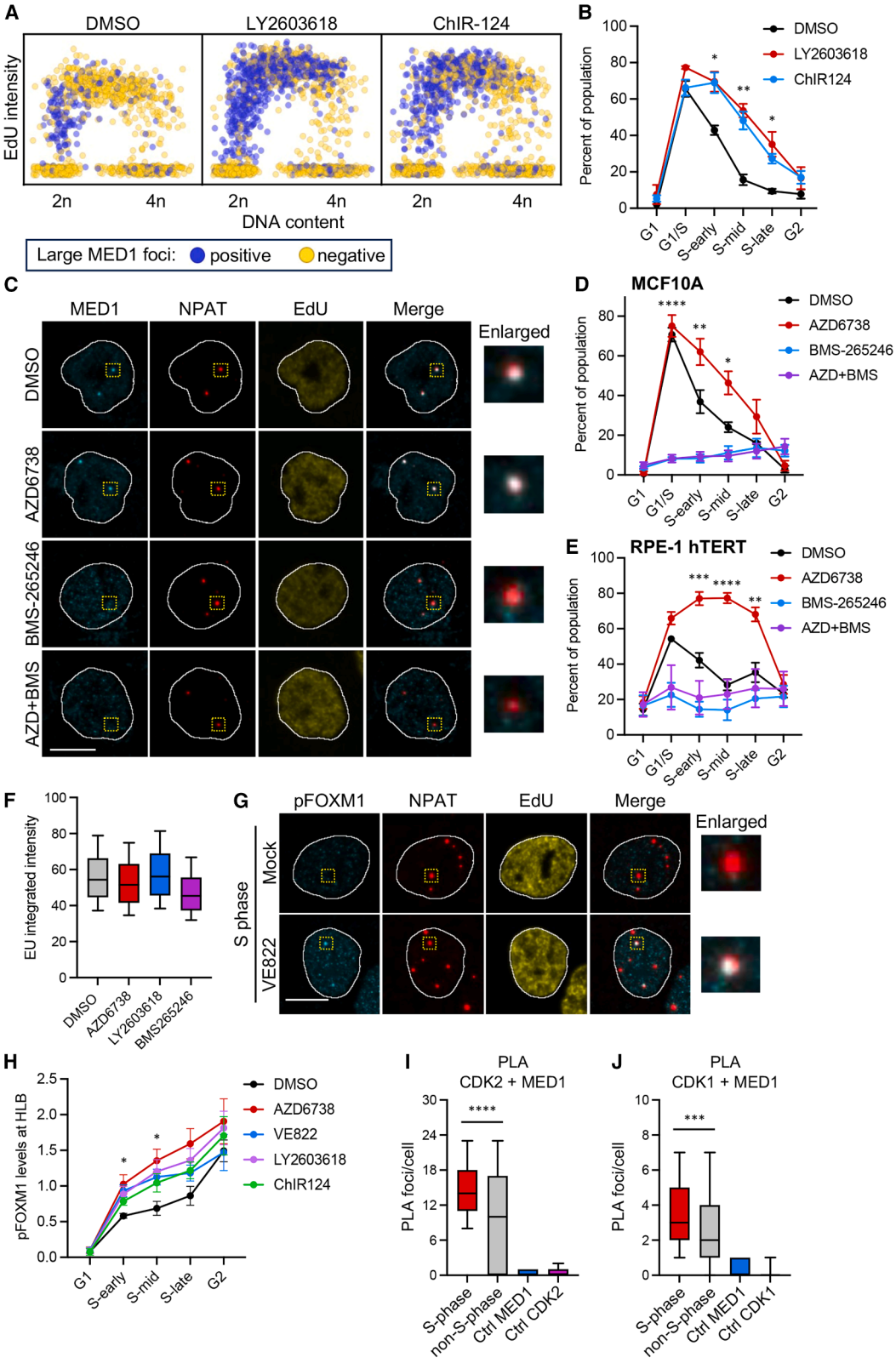

(legend on next page)

unchanged, though H2A levels were elevated in cells with pan-nuclear staining (Figure S6A).

To determine if elevated linker histone content was required for pan-nuclear DNA damage formation, we performed individual knockdowns of each linker histone (Figures 6C and S6B) prior to ATR and CHK1 inhibition. Knockdown of either H1.1 or H1.3 almost completely rescued γH2AX levels (Figure 6D). H1.2 and H1.4 knockdown caused a partial rescue of γH2AX levels, and intriguingly, H1.5 knockdown increased γH2AX (Figure S6C), indicating an imbalance in linker histones can lead to nucleus-wide DNA damage upon ATR-CHK1 inhibition.

We tested whether H1.1 and H1.3 knockdown could rescue RPA exhaustion and replication catastrophe. Like MED1, neither H1.1 nor H1.3 knockdown rescued replication catastrophe (Figures S6D and S6E), and in cells with ATR inhibition alone, H1.1 and H1.3 knockdown reduced γH2AX without lowering RPA levels on chromatin (Figure S6F). Furthermore, knockdown of these linker histones did not rescue CDC45 loading on chromatin in ATR-inhibited cells (Figure S6G). We note that H1.3 knockdown also lowered H1.1 levels. Thus, we cannot rule out the possibility that phenotypes associated with H1.3 knockdown are due to H1.1 loss (Figure S6H).

ATR-CHK1 controls linker H1.1 expression

We focused further molecular analyses on H1.1, as it had the highest content level in damaged cells, and its knockdown led to the strongest rescue of γH2AX levels. H1.1 knockdown slightly increased global transcription based on EU labeling of nascent RNA (Figure S6I), confirming that pan-nuclear DNA damage is not caused by broad changes to transcription. Knockdown of the different linker histones caused partial to no loss of EdU incorporation in S phase cells (Figure S6J). Though H1.1 knockdown did partially reduce EdU levels, H1.2 knockdown also reduced EdU levels without rescuing γH2AX, suggesting the pan-nuclear DNA damage is not affected by a small decrease in replication.

Transcription condensates promote gene activation, and given the elevated levels of H1.1, we suspected ATR and CHK1 inhibition caused overexpression of H1.1. RNA fluorescence *in situ* hybridization (RNA-FISH) revealed linker H1.1 expression was largely tied to the S phase (Figures 6E and 6F), and ATR and CHK1 inhibition further increased H1.1 expression 2-fold (Figures 6E and 6F). Aphidicolin treatment, which disrupts the HLB condensates (Figure S4D), completely down-regulated H1.1 expression (Figure S6K). Based on these results, we propose cells depend on ATR-CHK1 for precise control over transcription condensate dynamics at HLBs to prevent linker histone overexpression and subsequent DNA damage. In support of this, ectopic overexpression of H1.1-GFP triggered spontaneous DNA damage (Figure S6L).

MED1^{IDR} increases H1.1 expression and triggers global DNA damage in ATR-CHK1-inhibited cells

We sought to link the changes in MED1 foci dynamics to overexpression of H1.1. Of note, MED1 knockdown reduced H1.1 levels throughout the cell cycle, confirming an important role for MED1 in H1.1 expression (Figure 7A). MED1 localizes to transcription condensates through a process dependent on its large IDR (Figure 7B).[2,8] We cloned the MED1^{IDR} and the fluorescent mNeonGreen protein to create a hybrid mNeonGreen-MED1^{IDR} (NG-MED1^{IDR}) under the control of the doxycycline-inducible Tet-ON promoter and used this to generate a stable MCF10A cell line (Figure 7C). Upon doxycycline induction, live imaging of the fluorescent mNeonGreen reporter revealed NG-MED1^{IDR} to form foci in cells when expressed above a certain threshold (Figures S7A and S7B). Notably, the NG-MED1^{IDR} foci colocalized with NPAT, indicating the IDR was sufficient for localization to the HLB (Figure 7D).

Next, we grouped cells based on NG-MED1^{IDR} levels, ranging from negative (equal fluorescence signal to the uninduced control) to low, medium, and high (Figure S7C). Analysis of H1.1 content across the cell cycle (Figure S7D) revealed an approximate doubling of H1.1 content across S phase in both the uninduced and negative cell populations (Figure 7E), an expected increase as histone content should double across S phase. Strikingly, H1.1 content was elevated in cells with NG-MED1^{IDR} levels above the uninduced and negative cells, with H1.1 content highest in cells with the greatest NG-MED1^{IDR} levels (Figure 7E). Thus, MED1^{IDR} localizes to the HLB and amplifies the expression of H1.1, independent of the MED1 structured domain.

Figure 4. S phase checkpoint signaling controls transcription condensate dynamics

(A) Scatterplot of DAPI integrated intensity (linear scale) and EdU mean intensity (log_2 scale) in MCF10A cells treated with DMSO (mock), 2 μM LY2603618 (CHK1 inhibitor), or 250 nM ChIR-124 (CHK1 inhibitor) for 1 h. *2n* and 4n denote the DNA content. Cells positive for large MED1 foci (diameter > 0.7 μm) were colored purple, and negative cells were yellow.

(B) Line plots showing the percent of cells with large MED1 foci for each cell cycle phase. Cells were treated as in (A). Points and error bars are the mean and standard error, respectively, of 3 independent experiments. *$p < 0.05$, **$p < 0.01$.

(C) Representative images of MED1, NPAT, and EdU in early S phase MCF10A cells treated with DMSO (mock), 5 μM AZD6738 (ATR inhibitor), 5 μM BMS-265246 (CDK1/2 inhibitor), or both the ATR inhibitor and the CDK1/2 inhibitor for 1 h. Yellow boxes mark regions of enlarged condensates. Scale bar, 10 μm.

(D and E) Line plots showing the percent of MCF10A cells (D) and RPE1-hTERT cells (E) with large MED1 foci for each cell cycle phase. Cells were treated as in (C). Points and error bars are the mean and standard error, respectively, of 3 independent experiments. *$p < 0.05$, **$p < 0.01$, ***$p < 0.001$, ****$p < 0.0001$.

(F) Boxplots showing EU integrated intensity in MCF10A cells treated with DMSO, 5 μM AZD6738 (ATR inhibitor), 2 μM LY2603618 (CHK1 inhibitor), or 5 μM BMX265246 (CDK1/2 inhibitor) for 1 h.

(G) Representative images of pFOXM1 (T600), NPAT, and EdU in MCF10A cells treated with DMSO (mock) or 5 μM VE822 (ATR inhibitor) for 1 h. Yellow boxes mark regions of enlarged condensates. Scale bar, 10 μm.

(H) Line plots showing the levels of pFOXM1 (T600) in NPAT-marked HLBs measured by immunofluorescence. Cells were treated with DMSO (mock), 5 μM AZD6738 (ATR inhibitor), 5 μM VE822 (ATR inhibitor), 2 μM LY2603618 (CHK1 inhibitor), or 250 nM ChIR-124 (CHK1 inhibitor) for 1 h. Points and error bars are the mean and standard error, respectively, of 3 independent experiments. *$p < 0.05$.

(I) Boxplots showing the quantification of PLA foci of CDK2 and MED1 per cell. Ctrl MED1 and Ctrl CDK2 are single-antibody controls. ****$p < 0.0001$.

(J) Boxplots showing the quantification of PLA foci of CDK1 and MED1 per cell. Ctrl MED1 and Ctrl CDK1 are single-antibody controls. ***$p < 0.001$.

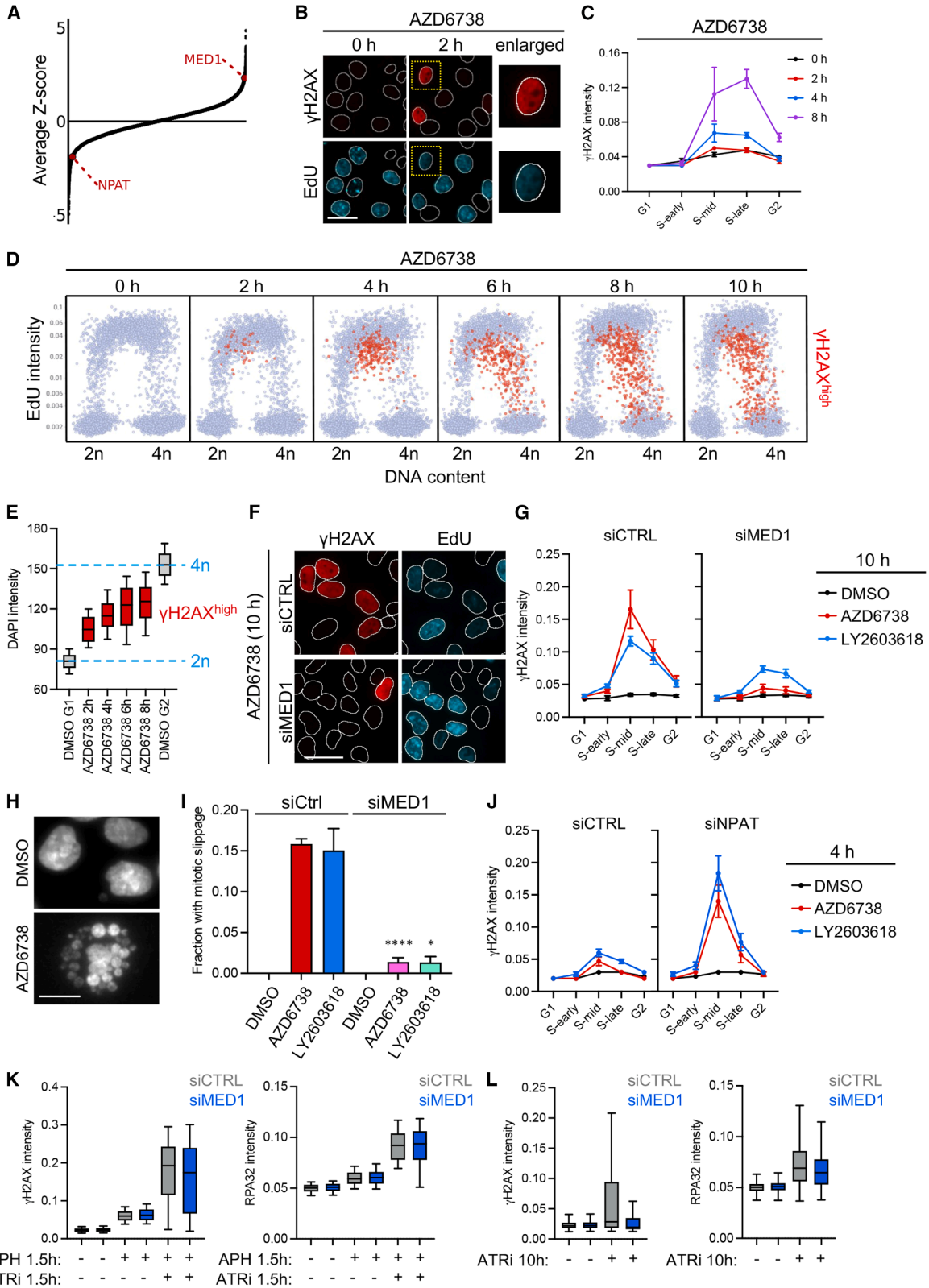

(legend on next page)

As a control, we mutated serine and threonine residues within the IDR to mimic the phosphorylation state of the MED1^{IDR} in S phase cells.[37] The IDR exhibits clustered phosphorylation in 5 separate regions, which we term "phospho-domains" (Figure S7E). Of these, only phospho-domain 2 (PD-2) is phosphorylated in S phase (Figure S7F; Table S1). Thus, for the MED1^{IDR} mutant control, we created S/T-to-D mutations in PD-2 and S/T-to-A mutations in the other PDs to mimic S phase phosphorylation (Figure S7G). Importantly, the mutant IDR failed to fully induce H1.1 expression (Figure 7E), suggesting phosphorylation of MED1^{IDR} may regulate its condensate properties.

Finally, we tested the impact of NG-MED1^{IDR} induction on pan-nuclear DNA damage in ATR-inhibited cells. Strikingly, increasing levels of NG-MED1^{IDR} triggered a corresponding increase in γH2AX pan-nuclear staining when ATR was inhibited (Figure 7F). Collectively, our data reveal the ATR-CHK1 pathway as a local regulator of transcription condensate dynamics at the HLB, controlling MED1 dissociation from the membrane-less compartment as cells undergo DNA replication. The precision of these dynamics fine-tunes linker histone expression, balances the pool of the different linker histones, and prevents nucleus-wide DNA damage.

DISCUSSION

Our study reveals the dynamics of large transcription condensates that appear precisely at the G1/S transition and dissolve during S phase progression. These transcription condensates localize to HLBs and couple the expression of histone genes with DNA replication.

Coordination of DNA replication and histone synthesis is driven by opposing S phase kinases. First, the appearance of MED1 foci at the G1/S transition is dependent on DDK and CDK1/2. These kinases initiate replication at the start of S phase, and thus, by localizing to HLBs and promoting condensate formation, they ensure replication and histone synthesis initiate simultaneously. Histone genes undergo a burst of transcription at the G1/S transition,[11] and we propose this is driven by the sudden appearance of large condensates at HLBs at the G1/S transition. Indeed, bursts in gene transcription have been linked to transcription condensates.[38]

Dissolution of transcription condensates in mid-S phase is governed by ATR and prevents hyper-transcription of histone genes, maintains a balanced pool of new histones, and safeguards genomic stability, highlighting transcription condensates as actively regulated assemblies across the cell cycle. Of note, it was recently shown that hyper-transcription of histone genes correlated with chromosome instability, tumor aggressiveness, and human cancer outcomes,[39] and accordingly, the effectiveness of ATR inhibitors as a cancer therapeutic may depend on the transcriptional state of the histone genes.

The nature of ATR enrichment in HLBs is unknown. As part of the DDR, ATR is recruited to RPA-coated single-stranded DNA.[40] Moreover, optogenetic studies have linked the DDR to condensate formation and ATR activation.[41–43] The recruitment of ATR to HLBs appears distinct from the DDR, as it occurs without γH2AX or RPA enrichment and does not involve ETAA1 or TOPBP1. Despite this, ATR is active within HLBs and suppresses CDK1 to prevent FOXM1 phosphorylation in S phase as part of the S/G2 checkpoint.[16,25,29]

Rather than responding to DNA lesions, ATR is recruited to HLBs in a transcription-dependent manner, where it binds to histone gene promoters and negatively regulates the transcriptional output of the linker H1 histones. What recruits ATR to promoters is an open question, though links between ATR and transcription have been described.[44,45] Mechanistically, ATR likely destabilizes multivalent MED1 interactions, gradually weakening MED1 foci across S phase. These findings support an emerging

Figure 5. Deregulation of HLB dynamics causes genome instability in ATR-CHK1-inhibited cells

(A) Average normalized *Z* score from a genome-wide CRISPR-Cas9 screen in ATR-inhibited cells.[35] MED1 and NPAT are highlighted to show MED1 knockout increases survival, whereas NPAT knockout decreases survival of ATR-inhibited cells. Averages were calculated from the normalized *Z* scores for MCF10A, HCT116, and HEK293 cells.

(B) Representative images of γH2AX and EdU in MCF10A cells treated with 5 μM AZD6738 for 2 h. Scale bar, 30 μm.

(C) Line plots showing γH2AX mean intensity measured by immunofluorescence. Cells were treated with 5 μM AZD6738 (ATR inhibitor) for 0–8 h. Points and error bars are the mean and standard error, respectively, of 3 independent experiments.

(D) Scatterplot of DAPI integrated intensity (linear scale) and EdU mean intensity (log_2 scale) in MCF10A cells treated with 5 μM AZD6738 (ATR inhibitor) for 0–10 h. 2*n* and 4n denote the DNA content. Cells positive for pan-nuclear γH2AX were colored red (γH2AX high). The threshold for pan-nuclear γH2AX is indicated in Figure S5A.

(E) Boxplots of the DAPI integrated intensity in cells from (D) with pan-nuclear γH2AX (red-shaded boxes [red dots in D]). Gray-shaded boxes show the DAPI intensity in DMSO-treated G1 and G2 cells. G1 and G2 cells were used to mark the 2*n* and 4n DNA content, respectively.

(F) Representative images of γH2AX and EdU in MCF10A cells transfected with siCTRL or siMED1 and treated with 5 μM AZD6738 for 10 h. Scale bar, 30 μm.

(G) Line plots showing γH2AX mean intensity measured by immunofluorescence in MCF10A cells transfected with non-targeting control siRNAs (siCTRL) or siMED1 and treated with DMSO, AZD6738 (5 μM), or LY2603618 (2 μM) for 10 h. Points and error bars are the mean and standard error, respectively, of 3 independent experiments.

(H) Representative images of DAPI-stained nuclei in MCF10A cells treated with DMSO or 5 μM AZD6738 for 20 h. The image on the right shows a cell with mitotic slippage. Scale bar, 15 μm.

(I) Quantification of the fraction of all cells with mitotic slippage in immunofluorescence in MCF10A cells transfected with siCTRL or siMED1 and treated with DMSO, AZD6738 (5 μM), or LY2603618 (2 μM) for 20 h. Columns and error bars are the mean and standard error, respectively, of 3 independent experiments. $^{*}p < 0.05$, $^{****}p < 0.0001$.

(J) Line plots showing γH2AX mean intensity measured by immunofluorescence in MCF10A cells transfected with siCTRL or siNPAT and treated with DMSO, AZD6738 (5 μM), or LY2603618 (2 μM) for 4 h. Points and error bars are the mean and standard error, respectively, of 3 independent experiments.

(K) Boxplots showing chromatin-bound (pre-extracted) γH2AX and RP32 mean intensity in S phase cells transfected with siCTRL (gray-shaded boxes) or siMED1 (blue-shaded boxes) and then treated for 1.5 h with 5 μM aphidicolin (APH) or with combined 5 μM APH and 5 μM AZD6738 (ATRi). Data related to Figure S5K.

(L) Boxplots are the same as (K), but cells were treated for 10 h only with 5 μM AZD6738 (ATRi). Data related to Figure S5K.

CellPress
OPEN ACCESS

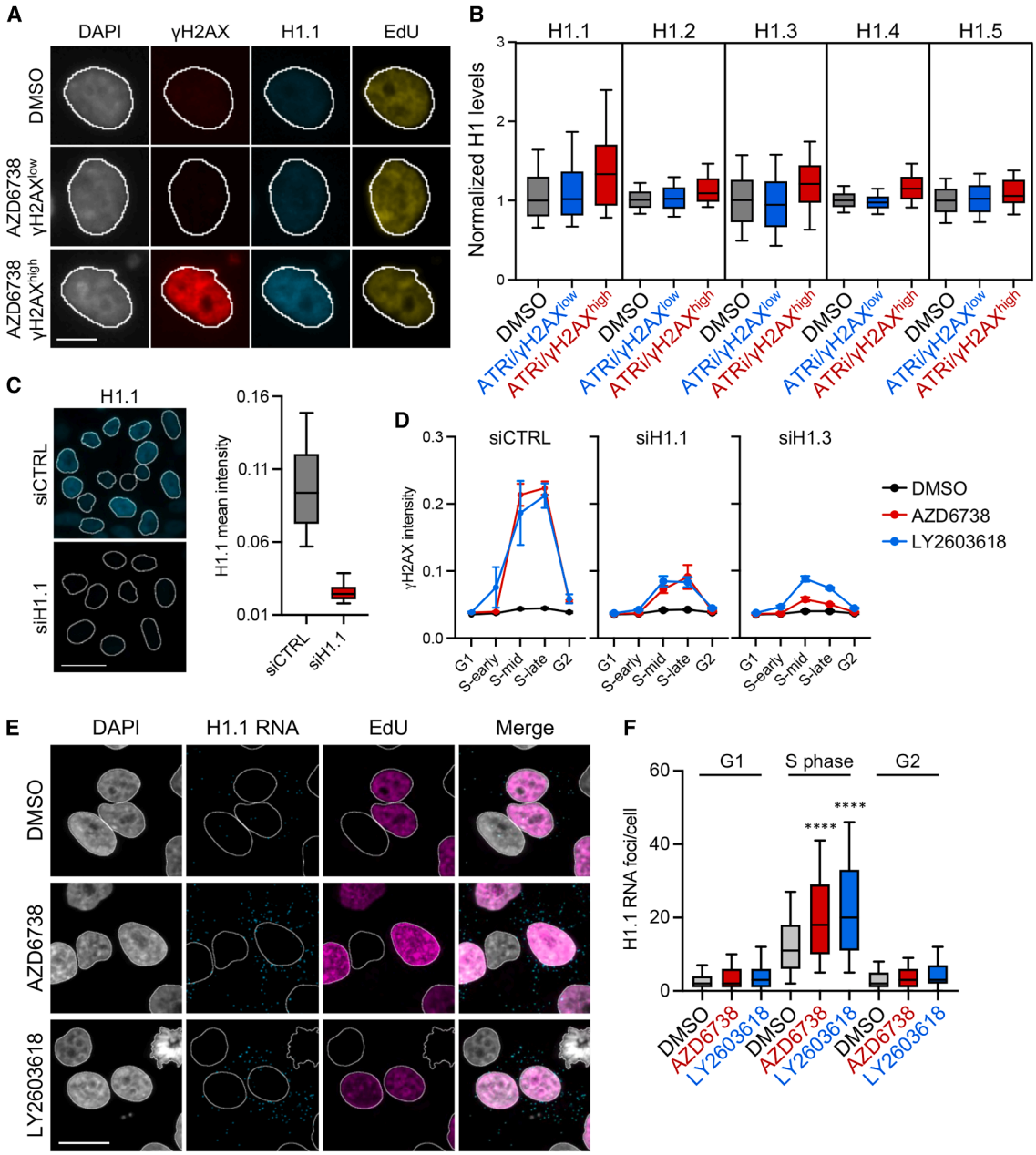

Figure 6. Hyper-transcription of linker histone H1.1 is associated with pan-nuclear DNA damage in ATR-inhibited cells

(A) Representative images of DAPI, γH2AX, H1.1, and EdU in MCF10A cells in early S phase treated with DMSO or 5 μM AZD6738 for 2 h. An AZD6738-treated cell with pan-nuclear γH2AX is shown in the third row. Note the elevated H1.1 intensity. Scale bar, 10 μm.

(B) Boxplots of linker histone H1 levels in MCF10A cells in early S phase treated with DMSO or 5 μM AZD6738 for 2 h. AZD6738-treated cells are split into groups either with normal γH2AX staining or with pan-nuclear γH2AX staining. The boxplots are split into five different groups to indicate normalized H1 levels for each of the five linkers (H1.1, H1.2, H1.3, H1.4, and H1.5).

(C) Representative images of H1.1 in MCF10A cells transfected with siCTRL or siH1.1 (scale bar, 30 μm), and boxplots of the H1.1 mean intensity showing strong knockdown with siH1.1.

(D) Line plots showing γH2AX mean intensity measured by immunofluorescence in MCF10A cells transfected with siCTRL, siH1.1, or siH1.3 and treated with DMSO, AZD6738 (5 μM), or LY2603618 (2 μM) for 8 h. Points and error bars are the mean and standard error, respectively, of 3 independent experiments.

(E) Representative images of H1.1 RNA-FISH, EdU, and DAPI in MCF10A cells treated with DMSO, AZD6738 (5 μM), or LY2603618 (2 μM) for 4 h. Scale bar, 20 μm.

(F) Boxplots of H1.1 RNA-FISH foci/cell across the cell cycle in MCF10A cells treated as in (E). ****$p < 0.0001$.

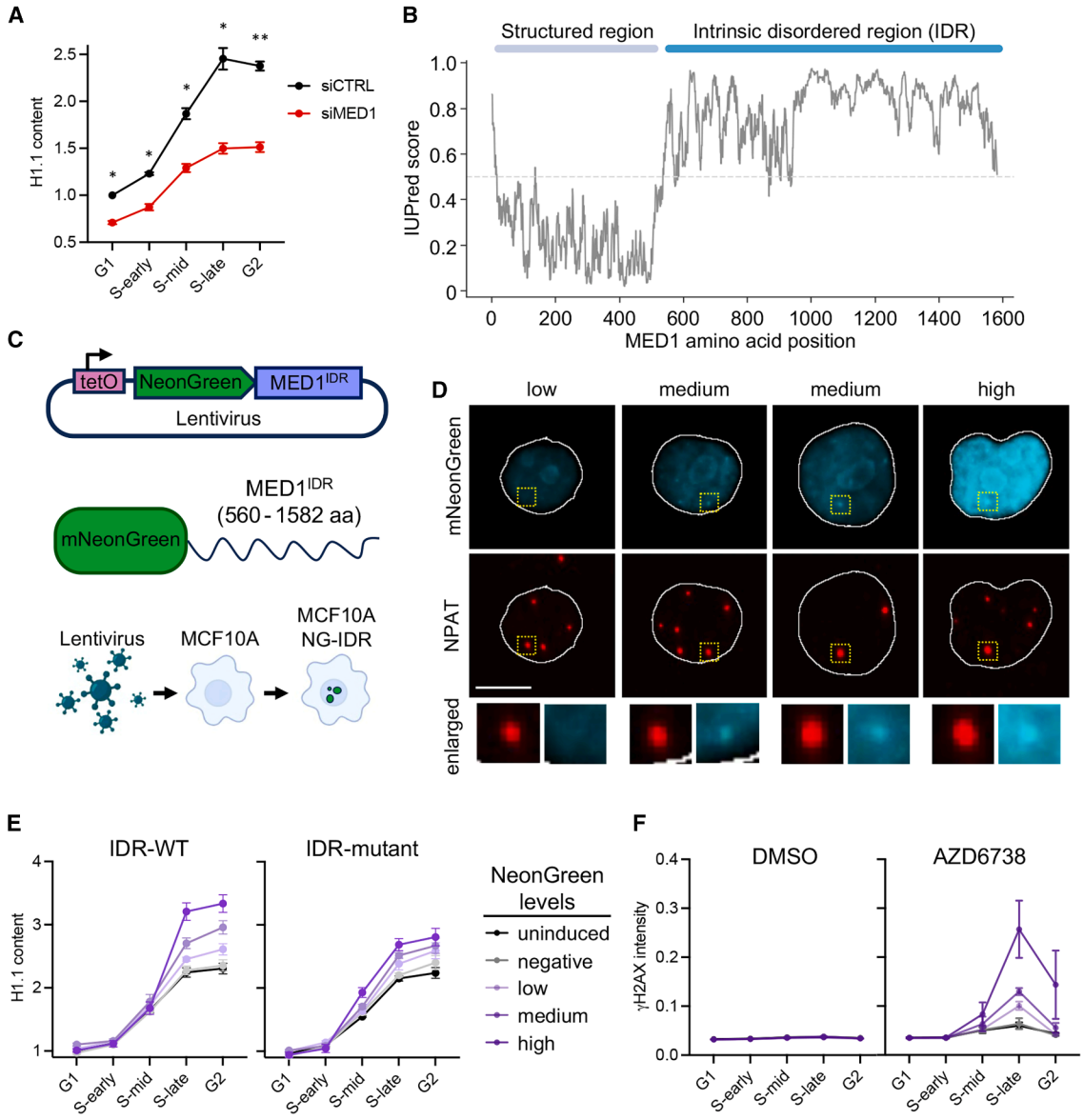

Figure 7. Transcription condensates amplify linker histone expression, causing sensitivity to ATR inhibition

(A) Line plots showing H1.1 content (normalized H1.1 intensity to G1 phase) measured by immunofluorescence in MCF10A cells transfected with siCTRL or siMED1. Points and error bars are the mean and standard error, respectively, of 3 independent experiments. *$p < 0.05$ and **$p < 0.01$.

(B) Line plot illustrating the intrinsic unstructured protein prediction score for each residue of the MED1 sequence. Defined regions of the protein, structured and IDRs, are indicated on top of the plot.

(C) Schematic representation of the fluorescent reporter protein, mNeonGreen (NG), fused to the MED1^{IDR} (560–1,582 aa) in a doxycycline-inducible lentiviral vector. Stable MCF10A cells were generated.

(D) Representative images of mNeonGreen and NPAT in MCF10A cells expressing mNeonGreen fused to MED1^{IDR}. Images show increases in levels of mNeonGreen from low to high levels. Note that mNeonGreen forms foci that overlap with NPAT in cells with medium and high levels of mNeonGreen. Scale bar, 10 μm.

(E) Line plots showing H1.1 content measured by immunofluorescence in MCF10A cells with increasing levels of mNeonGreen-MED^{IDR}-WT or mNeonGreen-MED^{IDR}-mutant. Thresholds for the different levels of mNeonGreen are shown in Figure S7C, and cell-cycle gates are shown in Figure S7D. Points and error bars are the mean and standard error, respectively, of 6 independent experiments.

(F) Line plots showing γH2AX mean intensity measured by immunofluorescence in MCF10A cells increasing levels of mNeonGreen and treated with DMSO or 5 μM AZD6738 for 9 h. Points and error bars are the mean and standard error, respectively, of 3 independent experiments.

paradigm suggesting ATR plays broader roles in S phase beyond the replication stress response, acting to coordinate replication with other fundamental processes.

Failure to regulate transcription condensates at HLBs results in overexpression of linker histone genes—most notably the linker histones H1.1 and H1.3. Overexpression correlates with pan-nuclear DNA damage in ATR-CHK1-inhibited cells. Interestingly, the DNA damage does not stem from general transcriptional or replicative failure but specifically from histone stoichiometry imbalance, suggesting that excess linker histones destabilize the genome.

It is unknown why an increase in H1.1 and H1.3 would lead to widespread DNA damage. Linker histones influence chromatin architecture and compaction,[46] and this, in turn, affects transcription and replication. We speculate H1.1 and H1.3 overexpression may alter chromatin architecture, causing replication stress and thus sensitivity to ATR or CHK1 inhibition. H1 depletion causes replication fork stalling and DNA damage due to transcription-replication conflicts, a defect likely caused by an aberrant opening of chromatin.[47] To date, little is known about the specific functions of H1.1 and H1.3, and thus, further research is needed to determine why their overexpression leads to DNA damage. Nonetheless, the change in H1.1 and H1.3 creates a linker histone pool imbalance, a phenotype linked to genome instability, cGAS activation, and immune dysfunction.[48]

Altogether, these findings position the HLB as an underappreciated hub of the ATR pathway and establish transcription condensate dynamics as critically important for genome stability. The S phase is a period of rapid change to chromatin, and without precise control over transcription condensates, genome-wide DNA damage would lead to loss of viability. This precision is achieved, in part, through opposing kinases (i.e., ATR-CHK1 vs. CDK1/2), balancing the pool of histone genes, and safeguarding genome integrity.

Limitations of the study

In Figure 2, we show that ATR is recruited to the HLB in a transcription-dependent manner. We also show that ATR binds to the histone gene promoters, suggesting a previously undescribed mechanism for ATR recruitment to chromatin. However, we cannot exclude the possibility that low levels of DNA damage within the HLB recruit ATR to the compartment.

In Figure 3, we use 1,6-hexanediol to interrogate the biophysical properties of the MED1 foci; however, there are caveats with the use of this alcohol to study the properties of condensates in living cells.[7] While it has been reported to differentiate liquid-like from solid-like assemblies,[22] 1,6-hexanediol does not disrupt all interactions that induce phase separation.[7] 1,6-hexanediol also alters the permeability of cell membranes and can induce artifacts.[22] Thus, caution is needed when interpreting the results in Figure 3.

A limitation of our study is that we do not use the *in vitro* droplet assay. The reason for this is because the role of ATR, and other kinases, to regulate MED1 phase separation is highly context specific. It is specific to mid-to-late-S phase, and it is specific to the HLB. To reconstitute this specific context and include purified ATR with the correct activation status is not trivial, and the number of variables in such an approach would make interpretations difficult.

In Figure 5, we show that MED1 induces DNA damage in ATR-inhibited cells. We interpret this as evidence that ATR's role of regulating MED1 at the HLB is part of its essential function. However, it is difficult to distinguish MED1 function at HLBs from other functions throughout the nucleus, and given this, the knockdown of MED1 could rescue damage caused by ATR inhibition via other mechanisms that do not involve the HLB.

RESOURCE AVAILABILITY

Lead contact

Further information and requests for resources and reagents should be directed to and will be fulfilled by the lead contact, Joshua C. Saldivar (saldivaj@ohsu.edu).

Materials availability

Plasmids generated in this study are available from the lead contact upon request.

Data and code availability

- Imaging data are available on Mendeley Data: 10.17632/w7b89wc4tg.1.
- Original CellProfiler pipelines have been deposited in GitHub and archived at Zenodo (DOI: 10.5281/zenodo.18040849).
- Any additional information required to reanalyze the data reported in this paper is available from the lead contact upon request.

ACKNOWLEDGMENTS

We thank members of the Saldivar laboratory for helpful discussions on the work presented in this paper. C.O.M. and J.L. are funded by an award from the Cancer Early Detection Advanced Research Center (CEDAR). C.S. is funded by a National Institutes of Health (NIH) institutional training grant (T32GM142619). Work in the Hamperl laboratory is funded by the Helmholtz Association, the German Research Foundation (DFG; Project ID 213249687; SFB 1064), and the European Research Council (ERC Starting Grant 852798). J.C.S. is funded by CEDAR, an NIH grant (GM147710), and a Career Development Award to Promote Diversity and Inclusion from the American Association for Cancer Research (AACR; 21-20-26-SALD). The research reported in this publication used computational infrastructure supported by the Office of Research Infrastructure Programs, Office of the Director, NIH, under award number S10OD034224. The content is solely the responsibility of the authors and does not necessarily represent the official views of the NIH.

AUTHOR CONTRIBUTIONS

Conceptualization, C.O.M. and J.C.S.; methodology, C.O.M., J.L., J.C.S., and S.H.; investigation, C.O.M., C.S., E.H., M.J.M., P.R., J.L., M.W., and J.C.S.; writing – original draft, J.C.S. and C.O.M.; writing – review & editing, J.C.S., S.H., and C.O.M.; funding acquisition, C.O.M., S.H., and J.C.S.; resources, J.C.S. and S.H.; supervision, J.C.S. and S.H.

DECLARATION OF INTERESTS

The authors declare no competing interests.

STAR★METHODS

Detailed methods are provided in the online version of this paper and include the following:

- KEY RESOURCES TABLE
- EXPERIMENTAL MODEL AND STUDY PARTICIPANT DETAILS

SUPPLEMENTAL INFORMATION

Supplemental information can be found online at https://doi.org/10.1016/j.molcel.2026.01.005.

Received: July 25, 2025
Revised: November 5, 2025
Accepted: January 5, 2026
Published: February 4, 2026

REFERENCES

1. Bhat, P., Honson, D., and Guttman, M. (2021). Nuclear compartmentalization as a mechanism of quantitative control of gene expression. Nat. Rev. Mol. Cell Biol. *22*, 653–670. https://doi.org/10.1038/s41580-021-00387-1.
2. Sabari, B.R., Dall'Agnese, A., Boija, A., Klein, I.A., Coffey, E.L., Shrinivas, K., Abraham, B.J., Hannett, N.M., Zamudio, A.V., Manteiga, J.C., et al. (2018). Coactivator condensation at super-enhancers links phase separation and gene control. Science *361*, eaar3958. https://doi.org/10.1126/science.aar3958.
3. Cho, W.K., Spille, J.H., Hecht, M., Lee, C., Li, C., Grube, V., and Cisse, I.I. (2018). Mediator and RNA polymerase II clusters associate in transcription-dependent condensates. Science *361*, 412–415. https://doi.org/10.1126/science.aar4199.
4. Hnisz, D., Shrinivas, K., Young, R.A., Chakraborty, A.K., and Sharp, P.A. (2017). A Phase Separation Model for Transcriptional Control. Cell *169*, 13–23. https://doi.org/10.1016/j.cell.2017.02.007.
5. Guo, Y.E., Manteiga, J.C., Henninger, J.E., Sabari, B.R., Dall'Agnese, A., Hannett, N.M., Spille, J.H., Afeyan, L.K., Zamudio, A.V., Shrinivas, K., et al. (2019). Pol II phosphorylation regulates a switch between transcriptional and splicing condensates. Nature *572*, 543–548. https://doi.org/10.1038/s41586-019-1464-0.
6. Li, P., Banjade, S., Cheng, H.C., Kim, S., Chen, B., Guo, L., Llaguno, M., Hollingsworth, J.V., King, D.S., Banani, S.F., et al. (2012). Phase transitions in the assembly of multivalent signalling proteins. Nature *483*, 336–340. https://doi.org/10.1038/nature10879.
7. Alberti, S., Gladfelter, A., and Mittag, T. (2019). Considerations and Challenges in Studying Liquid-Liquid Phase Separation and Biomolecular Condensates. Cell *176*, 419–434. https://doi.org/10.1016/j.cell.2018.12.035.
8. Sabari, B.R., Dall'Agnese, A., and Young, R.A. (2020). Biomolecular Condensates in the Nucleus. Trends Biochem. Sci. *45*, 961–977. https://doi.org/10.1016/j.tibs.2020.06.007.
9. Hamperl, S., and Cimprich, K.A. (2016). Conflict Resolution in the Genome: How Transcription and Replication Make It Work. Cell *167*, 1455–1467. https://doi.org/10.1016/j.cell.2016.09.053.
10. Duronio, R.J., and Marzluff, W.F. (2017). Coordinating cell cycle-regulated histone gene expression through assembly and function of the Histone Locus Body. RNA Biol. *14*, 726–738. https://doi.org/10.1080/15476286.2016.1265198.
11. Armstrong, C., Passanisi, V.J., Ashraf, H.M., and Spencer, S.L. (2023). Cyclin E/CDK2 and feedback from soluble histone protein regulate the S phase burst of histone biosynthesis. Cell Rep. *42*, 112768. https://doi.org/10.1016/j.celrep.2023.112768.
12. Marzluff, W.F., Wagner, E.J., and Duronio, R.J. (2008). Metabolism and regulation of canonical histone mRNAs: life without a poly(A) tail. Nat. Rev. Genet. *9*, 843–854. https://doi.org/10.1038/nrg2438.
13. Boija, A., Klein, I.A., Sabari, B.R., Dall'Agnese, A., Coffey, E.L., Zamudio, A.V., Li, C.H., Shrinivas, K., Manteiga, J.C., Hannett, N.M., et al. (2018). Transcription Factors Activate Genes through the Phase-Separation Capacity of Their Activation Domains. Cell *175*, 1842–1855.e16. https://doi.org/10.1016/j.cell.2018.10.042.
14. Klein, I.A., Boija, A., Afeyan, L.K., Hawken, S.W., Fan, M., Dall'Agnese, A., Oksuz, O., Henninger, J.E., Shrinivas, K., Sabari, B.R., et al. (2020). Partitioning of cancer therapeutics in nuclear condensates. Science *368*, 1386–1392. https://doi.org/10.1126/science.aaz4427.
15. Jaeger, M.G., Schwalb, B., Mackowiak, S.D., Velychko, T., Hanzl, A., Imrichova, H., Brand, M., Agerer, B., Chorn, S., Nabet, B., et al. (2020). Selective Mediator dependence of cell-type-specifying transcription. Nat. Genet. *52*, 719–727. https://doi.org/10.1038/s41588-020-0635-0.
16. Saldivar, J.C., Hamperl, S., Bocek, M.J., Chung, M., Bass, T.E., Cisneros-Soberanis, F., Samejima, K., Xie, L., Paulson, J.R., Earnshaw, W.C., et al. (2018). An intrinsic S/G2 checkpoint enforced by ATR. Science *361*, 806–810. https://doi.org/10.1126/science.aap9346.
17. Toledo, L.I., Altmeyer, M., Rask, M.B., Lukas, C., Larsen, D.H., Povlsen, L.K., Bekker-Jensen, S., Mailand, N., Bartek, J., and Lukas, J. (2013). ATR prohibits replication catastrophe by preventing global exhaustion of RPA. Cell *155*, 1088–1103. https://doi.org/10.1016/j.cell.2013.10.043.
18. Saldivar, J.C., Cortez, D., and Cimprich, K.A. (2017). The essential kinase ATR: ensuring faithful duplication of a challenging genome. Nat. Rev. Mol. Cell Biol. *18*, 622–636. https://doi.org/10.1038/nrm.2017.67.
19. Nizami, Z., Deryusheva, S., and Gall, J.G. (2010). The Cajal body and histone locus body. Cold Spring Harb. Perspect. Biol. *2*, a000653. https://doi.org/10.1101/cshperspect.a000653.
20. Tatomer, D.C., Terzo, E., Curry, K.P., Salzler, H., Sabath, I., Zapotoczny, G., McKay, D.J., Dominski, Z., Marzluff, W.F., and Duronio, R.J. (2016). Concentrating pre-mRNA processing factors in the histone locus body facilitates efficient histone mRNA biogenesis. J. Cell Biol. *213*, 557–570. https://doi.org/10.1083/jcb.201504043.
21. Solvie, D., Baluapuri, A., Uhl, L., Fleischhauer, D., Endres, T., Papadopoulos, D., Aziba, A., Gaballa, A., Mikicic, I., Isaakova, E., et al. (2022). MYC multimers shield stalled replication forks from RNA polymerase. Nature *612*, 148–155. https://doi.org/10.1038/s41586-022-05469-4.
22. Kroschwald, S., Maharana, S., and Simon, A. (2017). Hexanediol: a chemical probe to investigate the material properties of membrane-less compartments. Matters. https://doi.org/10.19185/matters.201702000010.
23. Liu, X., Jiang, S., Ma, L., Qu, J., Zhao, L., Zhu, X., and Ding, J. (2021). Time-dependent effect of 1,6-hexanediol on biomolecular condensates and 3D chromatin organization. Genome Biol. *22*, 230. https://doi.org/10.1186/s13059-021-02455-3.
24. Daigh, L.H., Liu, C., Chung, M., Cimprich, K.A., and Meyer, T. (2018). Stochastic Endogenous Replication Stress Causes ATR-Triggered Fluctuations in CDK2 Activity that Dynamically Adjust Global DNA Synthesis Rates. Cell Syst. *7*, 17–27.e3. https://doi.org/10.1016/j.cels.2018.05.011.

25. Lemmens, B., Hegarat, N., Akopyan, K., Sala-Gaston, J., Bartek, J., Hochegger, H., and Lindqvist, A. (2018). DNA Replication Determines Timing of Mitosis by Restricting CDK1 and PLK1 Activation. Mol. Cell *71*, 117–128.e3. https://doi.org/10.1016/j.molcel.2018.05.026.

26. Ma, T., Van Tine, B.A., Wei, Y., Garrett, M.D., Nelson, D., Adams, P.D., Wang, J., Qin, J., Chow, L.T., and Harper, J.W. (2000). Cell cycle-regulated phosphorylation of p220(NPAT) by cyclin E/Cdk2 in Cajal bodies promotes histone gene transcription. Genes Dev. *14*, 2298–2313. https://doi.org/10.1101/gad.829500.

27. Zhao, J., Dynlacht, B., Imai, T., Hori, T., and Harlow, E. (1998). Expression of NPAT, a novel substrate of cyclin E-CDK2, promotes S-phase entry. Genes Dev. *12*, 456–461. https://doi.org/10.1101/gad.12.4.456.

28. Zhao, J., Kennedy, B.K., Lawrence, B.D., Barbie, D.A., Matera, A.G., Fletcher, J.A., and Harlow, E. (2000). NPAT links cyclin E-Cdk2 to the regulation of replication-dependent histone gene transcription. Genes Dev. *14*, 2283–2297. https://doi.org/10.1101/gad.827700.

29. Branigan, T.B., Kozono, D., Schade, A.E., Deraska, P., Rivas, H.G., Sambel, L., Reavis, H.D., Shapiro, G.I., D'Andrea, A.D., and DeCaprio, J.A. (2021). MMB-FOXM1-driven premature mitosis is required for CHK1 inhibitor sensitivity. Cell Rep. *34*, 108808. https://doi.org/10.1016/j.celrep.2021.108808.

30. Zonderland, G., Vanzo, R., Gadi, S.A., Martín-Doncel, E., Coscia, F., Mund, A., Lerdrup, M., Benada, J., Boos, D., and Toledo, L. (2022). The TRESLIN-MTBP complex couples completion of DNA replication with S/G2 transition. Mol. Cell *82*, 3350–3365.e7. https://doi.org/10.1016/j.molcel.2022.08.006.

31. Brown, E.J., and Baltimore, D. (2000). ATR disruption leads to chromosomal fragmentation and early embryonic lethality. Genes Dev. *14*, 397–402. https://doi.org/10.1101/gad.14.4.397.

32. Cortez, D., Guntuku, S., Qin, J., and Elledge, S.J. (2001). ATR and ATRIP: partners in checkpoint signaling. Science *294*, 1713–1716. https://doi.org/10.1126/science.1065521.

33. de Klein, A., Muijtjens, M., van Os, R., Verhoeven, Y., Smit, B., Carr, A.M., Lehmann, A.R., and Hoeijmakers, J.H. (2000). Targeted disruption of the cell-cycle checkpoint gene ATR leads to early embryonic lethality in mice. Curr. Biol. *10*, 479–482. https://doi.org/10.1016/s0960-9822(00)00447-4.

34. Cimprich, K.A., and Cortez, D. (2008). ATR: an essential regulator of genome integrity. Nat. Rev. Mol. Cell Biol. *9*, 616–627. https://doi.org/10.1038/nrm2450.

35. Wang, C., Wang, G., Feng, X., Shepherd, P., Zhang, J., Tang, M., Chen, Z., Srivastava, M., McLaughlin, M.E., Navone, N.M., et al. (2019). Genome-wide CRISPR screens reveal synthetic lethality of RNASEH2 deficiency and ATR inhibition. Oncogene *38*, 2451–2463. https://doi.org/10.1038/s41388-018-0606-4.

36. Buisson, R., Boisvert, J.L., Benes, C.H., and Zou, L. (2015). Distinct but Concerted Roles of ATR, DNA-PK, and Chk1 in Countering Replication Stress during S Phase. Mol. Cell *59*, 1011–1024. https://doi.org/10.1016/j.molcel.2015.07.029.

37. Olsen, J.V., Vermeulen, M., Santamaria, A., Kumar, C., Miller, M.L., Jensen, L.J., Gnad, F., Cox, J., Jensen, T.S., Nigg, E.A., et al. (2010). Quantitative phosphoproteomics reveals widespread full phosphorylation site occupancy during mitosis. Sci. Signal. *3*, ra3. https://doi.org/10.1126/scisignal.2000475.

38. Du, M., Stitzinger, S.H., Spille, J.H., Cho, W.K., Lee, C., Hijaz, M., Quintana, A., and Cissé, I.I. (2024). Direct observation of a condensate effect on super-enhancer controlled gene bursting. Cell *187*, 331–344.e17. https://doi.org/10.1016/j.cell.2023.12.005.

39. Henikoff, S., Zheng, Y., Paranal, R.M., Xu, Y., Greene, J.E., Henikoff, J.G., Russell, Z.R., Szulzewsky, F., Thirimanne, H.N., Kugel, S., et al. (2025). RNA polymerase II at histone genes predicts outcome in human cancer. Science *387*, 737–743. https://doi.org/10.1126/science.ads2169.

40. Zou, L., and Elledge, S.J. (2003). Sensing DNA damage through ATRIP recognition of RPA-ssDNA complexes. Science *300*, 1542–1548. https://doi.org/10.1126/science.1083430.

41. Egger, T., Morano, L., Blanchard, M.P., Basbous, J., and Constantinou, A. (2024). Spatial organization and functions of Chk1 activation by TopBP1 biomolecular condensates. Cell Rep. *43*, 114064. https://doi.org/10.1016/j.celrep.2024.114064.

42. Frattini, C., Promonet, A., Alghoul, E., Vidal-Eychenie, S., Lamarque, M., Blanchard, M.P., Urbach, S., Basbous, J., and Constantinou, A. (2021). TopBP1 assembles nuclear condensates to switch on ATR signaling. Mol. Cell *81*, 1231–1245.e8. https://doi.org/10.1016/j.molcel.2020.12.049.

43. Spegg, V., Panagopoulos, A., Stout, M., Krishnan, A., Reginato, G., Imhof, R., Roschitzki, B., Cejka, P., and Altmeyer, M. (2023). Phase separation properties of RPA combine high-affinity ssDNA binding with dynamic condensate functions at telomeres. Nat. Struct. Mol. Biol. *30*, 451–462. https://doi.org/10.1038/s41594-023-00932-w.

44. Hamperl, S., Bocek, M.J., Saldivar, J.C., Swigut, T., and Cimprich, K.A. (2017). Transcription-Replication Conflict Orientation Modulates R-Loop Levels and Activates Distinct DNA Damage Responses. Cell *170*, 774–786.e19. https://doi.org/10.1016/j.cell.2017.07.043.

45. Matos, D.A., Zhang, J.M., Ouyang, J., Nguyen, H.D., Genois, M.M., and Zou, L. (2020). ATR Protects the Genome against R Loops through a MUS81-Triggered Feedback Loop. Mol. Cell *77*, 514–527.e4. https://doi.org/10.1016/j.molcel.2019.10.010.

46. Willcockson, M.A., Healton, S.E., Weiss, C.N., Bartholdy, B.A., Botbol, Y., Mishra, L.N., Sidhwani, D.S., Wilson, T.J., Pinto, H.B., Maron, M.I., et al. (2021). H1 histones control the epigenetic landscape by local chromatin compaction. Nature *589*, 293–298. https://doi.org/10.1038/s41586-020-3032-z.

47. Almeida, R., Fernández-Justel, J.M., Santa-María, C., Cadoret, J.C., Cano-Aroca, L., Lombraña, R., Herranz, G., Agresti, A., and Gómez, M. (2018). Chromatin conformation regulates the coordination between DNA replication and transcription. Nat. Commun. *9*, 1590. https://doi.org/10.1038/s41467-018-03539-8.

48. Uggenti, C., Lepelley, A., Depp, M., Badrock, A.P., Rodero, M.P., El-Daher, M.T., Rice, G.I., Dhir, S., Wheeler, A.P., Dhir, A., et al. (2020). cGAS-mediated induction of type I interferon due to inborn errors of histone pre-mRNA processing. Nat. Genet. *52*, 1364–1372. https://doi.org/10.1038/s41588-020-00737-3.

49. Schneider, C.A., Rasband, W.S., and Eliceiri, K.W. (2012). NIH Image to ImageJ: 25 years of image analysis. Nat. Methods *9*, 671–675. https://doi.org/10.1038/nmeth.2089.

50. Stirling, D.R., Swain-Bowden, M.J., Lucas, A.M., Carpenter, A.E., Cimini, B.A., and Goodman, A. (2021). CellProfiler 4: improvements in speed, utility and usability. BMC Bioinform. *22*, 433. https://doi.org/10.1186/s12859-021-04344-9.

51. Lalonde, M., Ummethum, H., Trauner, M., Ettinger, A., and Hamperl, S. (2024). An automated image analysis pipeline to quantify the coordination and overlap of transcription and replication activity in mammalian genomes. Methods Cell Biol. *182*, 199–219. https://doi.org/10.1016/bs.mcb.2023.05.012.

52. Ramírez, F., Ryan, D.P., Grüning, B., Bhardwaj, V., Kilpert, F., Richter, A.S., Heyne, S., Dündar, F., and Manke, T. (2016). deepTools2: a next generation web server for deep-sequencing data analysis. Nucleic Acids Res. *44*, W160–W165. https://doi.org/10.1093/nar/gkw257.

STAR★METHODS

KEY RESOURCES TABLE

REAGENT or RESOURCE	SOURCE	IDENTIFIER
Antibodies		
Mouse monoclonal anti-phospho-Histone H2A.X (Ser139)	Millipore Sigma	Cat# 05-636-I; RRID: AB_2755003
Rabbit monoclonal anti-phospho-ATR (Ser428)	Cell Signaling Technology	Cat# 2853S; RRID: AB_2290281
Rabbit monoclonal anti-TRAP220/MED1	Abcam	Cat# ab64965; RRID: AB_1142301
Mouse monoclonal anti-human NPAT	BD Biosciences	Cat# 611344; RRID: AB_398866
Rabbit monoclonal anti-phospho-FOXM1 (Thr600)	Cell Signaling Technology	Cat# 14655S; RRID: AB_2798557
Rabbit monoclonal anti-BRD4	Abcam	Cat# ab128874; RRID: AB_11145462
Rabbit monoclonal anti-RPA32/RPA2	Abcam	Cat# ab76420; RRID: AB_1524336
Rabbit polyclonal anti-RNA polymerase II CTD repeat YSPTSPS	Abcam	Cat# ab26721; RRID: AB_777726
Rabbit monoclonal anti-histone H1.1	Abcam	Cat# ab254394; RRID: AB_3677544
Rabbit polyclonal anti-histone H1.2	GeneTex	Cat# GTX122561; RRID: AB_11162414
Rabbit monoclonal anti-histone H1.3	Abcam	Cat# ab183736; RRID: AB_3722739
Rabbit monoclonal anti-histone H1.4 (D4J5Q)	Cell Signaling Technology	Cat# 41328S; RRID: AB_2799199
Rabbit polyclonal anti-histone H1.5	Abcam	Cat# ab18208; RRID: AB_470263
Rabbit monoclonal anti-histone H2A (D6O3A)	Cell Signaling Technology	Cat# 12349S; RRID: AB_2687875
Rabbit monoclonal anti-histone H2B (D2H6)	Cell Signaling Technology	Cat# 12364S; RRID: AB_2714167
Rabbit monoclonal anti-histone H3 (D1H2)	Cell Signaling Technology	Cat# 4499S; RRID: AB_10544537
Rabbit monoclonal anti-histone H4 (D2X4V)	Cell Signaling Technology	Cat# 13919S; RRID: AB_2798345
Mouse monoclonal anti-Human 53BP1	BD Biosciences	Cat# 612522; RRID: AB_2206766
Rabbit monoclonal anti-ATR (E1S3S)	Cell Signaling Technology	Cat# 13934S; RRID: AB_2798347
Mouse monoclonal anti-RNA polymerase II	Millipore Sigma	Cat# 05-623; RRID: AB_309852
Rabbit polyclonal anti-ATRIP	Cell Signaling Technology	Cat# 2737S; RRID: AB_823659
Rabbit monoclonal anti-TOPBP1	Cell Signaling Technology	Cat# 14342S; RRID: AB_2798456
Rabbit monoclonal anti-ETAA1	Cell Signaling Technology	Cat# 77021S; RRID: AB_3722741
Rabbit polyclonal anti-MED1	Cell Signaling Technology	Cat# 51613S; RRID: AB_2799397
Rabbit polyclonal anti-DBF4	Novus Biologicals	Cat# NBP2-55268; RRID: AB_3340515
Mouse monoclonal anti-CDK1	Novus Biologicals	Cat# NBP2-37626; RRID: AB_3296452
Mouse monoclonal anti-CDK2	Millipore Sigma	Cat# AMAB91497; RRID: AB_3731295
Alexa Fluor 568-conjugated goat anti-mouse IgG (H+L)	Invitrogen	Cat# A-11004 RRID: AB_2534072
Alexa Fluor 488-conjugated goat anti-rouse IgG (H+L)	Invitrogen	Cat# A-11008 RRID: AB_143165
Chemicals, peptides, and recombinant proteins		
Ceralasertib (AZD6738)	Selleck Chemicals	Cat# S7693
Berzosertib (VE-822)	Selleck Chemicals	Cat# S7102
Rabusertib (LY2603618)	Selleck Chemicals	Cat# S2626
CHIR-124	Selleck Chemicals	Cat# S2683
BMS-265246	Selleck Chemicals	Cat# S2014
RO3306	Selleck Chemicals	Cat# S7747
NU6140	Thermo Fisher Scientific	Cat# 33-011-0
Simurosertib (TAK-931)	MedChem Express	Cat# HY-100888
1,6 hexanediol	Millipore Sigma	Cat# 240117-50G
Polybrene	Millipore Sigma	Cat# TR-1003-G
Alexa Fluor™ 647 Azide, Triethylammonium Salt	Invitrogen	Cat# A10277
Alexa Fluor™ 594 Azide, Triethylammonium Salt	Invitrogen	Cat# A10270
Crystal Violet	Millipore Sigma	Cat# C0775

(*Continued on next page*)

Continued

REAGENT or RESOURCE	SOURCE	IDENTIFIER
DharmaFECT 1 Transfection Reagent	Horizon Discovery	Cat# T-2005-01
FuGENE® 6 transfection reagent	Promega	Cat# E2691
Lenti-X Concentrator	Takara Bio Inc.	Cat# 631232
Animal-Free Recombinant Human EGF	Peprotech	Cat# AF-100-15
Insulin from bovine pancreas	Millipore Sigma	Cat# I1882
Hydrocortisone	Millipore Sigma	Cat# H0888
Cholera Toxin from *Vibrio cholerae*	Millipore Sigma	Cat# C8052
Hygromycin B	Millipore Sigma	Cat# 10843555001
5-Ethynyl-2′-deoxyuridine (EdU)	Millipore Sigma	Cat# 900584-50MG
TrypLE Express Enzyme (1X), phenol red	Gibco	Cat# 12605010
Doxycycline Hyclate	Millipore Sigma	Cat# D5207-5G
Triton™ X-100	Millipore Sigma	Cat# T8787-50ML
Blasticidin	Invitrogen	Cat# ant-bl-1
Triptolide	ApexBio	Cat# A3891
5-ethynyluridine	ThermoFisher Scientific	Cat# E10345
Critical commercial assays		
Click-iT™ Cell Reaction buffer kit	Invitrogen	Cat# C10269
Duolink *In Situ* PLA probe anti-mouse PLUS	Millipore Sigma	Cat# DUO92001
Duolink *In Situ* PLA probe anti-rabbit MINUS	Millipore Sigma	Cat# DUO92005
Duolink *In Situ* Wash Buffers, Fluorescence	Millipore Sigma	Cat# DUO82049
Duolink *In Situ* Detection Reagents Green	Millipore Sigma	Cat# DUO92014
NEB Golden Gate Assembly Kit (BsmBI-v2)	New England Biolabs	Cat# E1602S
ViewRNA Cell Plus Assay Kit	ThermoFisher Scientific	Cat# 88-19000
Viewrna Cell Plus Probe Set, Alexa Fluor 488, HIST1H1A	ThermoFisher Scientific	Cat# VA4-3086709-VCP
Deposited Data		
Imaging data	This study	Mendeley: 10.17632/w7b89wc4tg.1
Experimental models: Cell lines		
Human: MCF10A cell line	ATCC	Cat# CRL-10317; RRID: CVCL_0598
Human: hTERT RPE-1	ATCC	Cat# CRL-4000; RRID: CVCL_4388
Human: HEK-293T	ATCC	Cat# CRL-3216; RRID: CVCL_0063
Oligonucleotides		
ON-TARGETplus Human MED1 siRNA	Horizon Discovery	Cat# L-004126-00-0005
ON-TARGETplus Human ATR siRNA	Horizon Discovery	Cat# J-003202-20-0002
ON-TARGETplus Non-targeting Pool	Horizon Discovery	Cat# D-001810-10-05
ON-TARGETplus Human MED4 siRNA	Horizon Discovery	Cat# L-020687-00-0005
ON-TARGETplus Human MED6 siRNA	Horizon Discovery	Cat# L-019963-00-0005
ON-TARGETplus Human MED12 siRNA	Horizon Discovery	Cat# L-009092-00-0005
ON-TARGETplus Human MED17 siRNA	Horizon Discovery	Cat# L-006312-00-0005
ON-TARGETplus Human MED18 siRNA	Horizon Discovery	Cat# L-020600-02-0005
ON-TARGETplus Human MED24 siRNA	Horizon Discovery	Cat# L-021247-00-0005
ON-TARGETplus Human MED26 siRNA	Horizon Discovery	Cat# L-011948-00-0005
ON-TARGETplus Human NPAT siRNA	Horizon Discovery	Cat# L-019599-01-0005
ON-TARGETplus Human H1.1 siRNA	Horizon Discovery	Cat# L-012045-02-0005
ON-TARGETplus Human H1.2 siRNA	Horizon Discovery	Cat# L-006630-00-0005
ON-TARGETplus Human H1.3 siRNA	Horizon Discovery	Cat# L-012046-02-0005
ON-TARGETplus Human H1.4 siRNA	Horizon Discovery	Cat# L-012048-02-0005
ON-TARGETplus Human H1.5 siRNA	Horizon Discovery	Cat# L-012049-02-0005

(*Continued on next page*)

Continued

REAGENT or RESOURCE	SOURCE	IDENTIFIER
Recombinant DNA		
Plasmid: pLenti CMV rtTA3 Blast (w756-1)	Addgene	Cat# 26429
Plasmid: mNeonGreen-mTurquoise2	Addgene	Cat# 98886
Plasmid: pCW57.1	Addgene	Cat# 41393
Plasmid: pWZL hygro Flag HA TRAP220 wt	Addgene	Cat# 17433
Plasmid: psPAX2	Addgene	Cat# 12260
Plasmid: pMD2.g	Addgene	Cat# 12259
Plasmid: pEGFP-H1.1	Addgene	Cat# 32894
Software and algorithms		
CellProfiler	Broad Institute	https://cellprofiler.org
ImageJ	Schneider et al.[49]	https://imagej.nih.gov/ij/
Python 3.9	Python Software Foundation	https://www.python.org/downloads/
GraphPad Prism 7.0	GraphPad Software	https://www.graphpad.com/
Spotfire	Cloud Software Group, Inc.	https://www.spotfire.com/
CellProfiler pipelines	This study	Zenodo: 10.5281/zenodo.18040849

EXPERIMENTAL MODEL AND STUDY PARTICIPANT DETAILS

MCF10A cells

Cells derived from an epithelial cell line that was isolated in 1984 from the mammary gland of a 36-year-old Caucasian female with fibrocystic breasts (ATCC, CRL-10317). MCF10A cells were cultured in DMEM:F12 (Thermo Fisher Scientific, 11320082) base medium, supplemented with 5% horse serum (Thermo Fisher Scientific, 16050122), 20 ng/ml EGF (Peprotech, AF-100-15), 10 μg/ml insulin (Millipore Sigma, I-1882), 0.5 mg/ml hydrocortisone (Millipore Sigma, H-0888), 100 ng/ml cholera toxin (Millipore Sigma, C-8052), and 1x penicillin/streptomycin (Thermo Fisher Scientific, 15140122). The cells were maintained in a humidified atmosphere with 5% CO_2 at 37°C.

hTERT RPE-1 cells

Cells obtained from an hTERT-immortalized retinal pigment epithelial cell line (ATCC, CRL-4000). RPE-1 cells were cultured in DMEM:F12 base medium supplemented with 10% fetal bovine serum (Thermo Fisher Scientific, A5256801), 0.1 mg/ml hygromycin B (Millipore Sigma, 10843555001), and 1x penicillin/streptomycin. The cells were maintained in a humidified atmosphere with 5% CO_2 at 37°C.

HEK-293T cells

Epithelial-like cell isolated from patient kidney cells expressing the SV40 large T antigen (ATCC, CRL-3216). HEK-293T cells were cultured in DMEM medium supplemented with 10% FBS and 1x penicillin/streptomycin in a humidified atmosphere with 5% CO_2 at 37°C. These cells were exclusively used for lentivirus production.

METHOD DETAILS

siRNA transfection

Cells were seeded at 8,000 cells per well in glass-bottom 96-well plates (Cellvis P96-1.5P) and reverse-transfected with either non-targeting siRNA (siCTRL; Horizon Discovery, D-001810-10-05) or siRNA targeting MED1 (siMED1; Horizon Discovery, L-004126-00-0005), ATR (siATR; Horizon Discovery, J-003202-20-0002), MED4 (siMED4; Horizon Discovery, L-020687-00-0005), MED6 (siMED6; Horizon Discovery, L-019963-00-0005), MED12 (siMED12; Horizon Discovery, L-009092-00-0005), MED17 (siMED17; Horizon Discovery, L-006312-00-0005), MED18 (siMED18; Horizon Discovery, L-020600-02-0005), MED24 (siMED24; Horizon Discovery, L-021247-00-0005), MED26 (siMED26; Horizon Discovery, L-011948-00-0005), NPAT (siNPAT; Horizon Discovery, L-019599-01-0005), H1.1 (siH1.1; Horizon Discovery, L-012045-02-0005), H1.2 (siH1.2; Horizon Discovery, L-006630-00-0005), H1.3 (siH1.3; Horizon Discovery, L-012046-02-0005), H1.4 (siH1.4; Horizon Discovery, L-012048-02-0005), or H1.5 (siH1.5; Horizon Discovery, L-012049-02-0005) at a concentration of 20 nM using DharmaFECT 1 (Horizon Discovery T-2005-01) following manufacturer's guidelines. 16 h post-transfection, the media was replaced with fresh growth media. Cells were analyzed 48 hours post-transfection.

Immunofluorescence staining

Cells were grown in 96-well plates with a glass-like polymer well-bottom (Cellvis P96-1.5P). For cell cycle analysis, cells were treated with 20 μM 5-ethynyl-2′-deoxyuridine (EdU) for 15 min prior to fixation. For experiments measuring nascent RNA, 100 μM 5-ethynyluridine (EU) was added to cells for 20 min prior to fixation. Cells were fixed with 4% paraformaldehyde (PFA) diluted in phosphate-buffered saline (PBS) for 10 min, permeabilized with ice-cold methanol for 10 min, washed 3 times with 1X PBS, and blocked with 1% bovine serum albumin (BSA) in PBS for 30 min at room temperature. For EdU or EU staining, the Click-iT reaction was performed following permeabilization using the Click-iT Cell Reaction Buffer kit (Invitrogen, C10269) and Alexa Fluor™ 647 Azide (Invitrogen, A10277) according to the manufacturer's guidelines. Specifically, cells were washed with 3% BSA/PBS and incubated with the Click-iT reaction mixture with 1 μg/ml of Alexa Fluor™ 647 Azide for 30 min with at room temperature on a bench rocker. After the Click-iT reaction, cells were washed with 3% BSA/PBS, followed by washed 3 times in 1X PBS, and blocked with 1% BSA in PBS for 30 min at room temperature. Following blocking, cells were incubated with primary antibodies. The primary antibodies used were anti-phospho-Histone H2A.X (1:1000, Millipore Sigma, 05-636-I), anti-phospho-ATR (1:500, Cell Signaling Technology, 2853S), anti-TRAP220/MED1 (1:1000, Abcam, ab64965), anti-RNAPOLII (1:1000, Abcam, ab26721), anti-NPAT (1:1000, BD Biosciences, 611344), anti-phospho-FOXM1 (1:250, Cell Signaling Technology, 14655S), anti-BRD4 (1:500, Abcam, ab128874), anti-RPA32/RPA2 (1:500, Abcam, ab76420), anti-Coilin (1:1000, Cell Signaling Technology, 14168T), anti-53BP1 (1:1000, Abcam, ab237174), anti-H1.1 (1:1000, Abcam, ab254394), anti-H1.2 (1:500, GeneTex, GTX122561), anti-H1.3 (1:1000, Abcam, ab183736), anti-H1.4 (1:500, Cell Signaling Technology, 41328), anti-H1.5 (1:1000, Abcam, ab18208), anti-H2A (1:500, Cell Signaling Technology, 12349), anti-H2B (1:500, Cell Signaling Technology, 12364), anti-H3 (1:500, Cell Signaling Technology, 4499S), anti-H4(1:500, Cell Signaling Technology, 13919), anti-ATRIP (1:500, Cell Signaling Techology, 2737S), anti-TOPBP1 (1:500, Cell Signaling Technology, 14342S), anti-ETAA1 (1:500, Cell Signaling Technology, 77021T), and anti-DBF4 (1:1000, Novus Biologicals, NBP2-55268). All the primary antibodies were diluted in 1% BSA/PBS and incubated overnight with constant agitation at 4°C. After incubation with primary antibodies, cells were washed 3 times in 1X PBS and co-stained with DAPI (5 μg/mL) and secondary antibodies The secondary antibodies, anti-rabbit Alexa Fluor 488 conjugated antibody (Thermo Fisher Scientific, A-11008) and anti-mouse Alexa Fluor 568 conjugated antibody (Thermo Fisher Scientific, A-11004), were diluted 1:1000 in 1% BSA and incubated for 1 h at room temperature on a bench rocker. Finally, cells were washed three times with 1X PBS before imaging.

Pre-extraction for immunofluorescence imaging of chromatin-bound proteins

Cells were grown in 96-well plates with a glass-like polymer well-bottom (Cellvis P96-1.5P). For cell cycle analysis, cells were treated with 20 μM 5-ethynyl-2′-deoxyuridine (EdU) for 15 min prior to pre-extraction. For pre-extraction, cells were briefly rinsed in PBS, and then pre-extracted with 0.5% triton-X for 1 minute followed by a minute wash in PBS. Cells were then fixed with 4% PFA for 10 minutes and immunofluorescence stained as described above.

Quantitative image-based cytometry and analysis

Cells were grown in 96-well plates with a glass-like polymer well-bottom (Cellvis P96-1.5P) and imaged on a fully-automated ImageXpress Micro Confocal Imaging System (Molecular Devices). Widefield images were captured using a 20X Ph1S Plan Fluor ELWD ADM 0.45 NA objective and a sCMOS camera. For foci detection and quantification, images were captured using a 40X APO LWD 1.15 NA water immersion objective, a 60-micron pinhole spinning disk, and a sCMOS camera. A z-series of 25 images at 0.2 micron step-sizes spanning the nuclear region was used to generate z-maximum projections, from which image analysis was performed. Image analysis was performed using CellProfiler (Broad Institute).[50] Intensity measurements were within a nuclear mask generated from DAPI-stained images. Background levels were determined for each fluorescence marker by assessing histogram plots of the signal intensities in each pixel across several images. The average background value across these images was then subtracted from the mean intensity of the given fluorescent marker in each cell. DNA content was determined using DAPI integrated intensity. Identification and quantification of foci (ATR foci, MED1 foci, and NPAT foci) was performed using an *in-house* developed CellProfiler pipeline. Identification and quantification of mitotic slippage were derived from the analysis of DAPI-stained images.

Proximity ligation assay

All steps were conducted at room temperature unless stated otherwise. Cells were seeded in a 96-well imaging plate (Ibidi, 89626) and treated with 10 μM EdU for 30 min before pre-extraction. Pre-extraction was done with 0.5 % Triton X-100 (Millipore Sigma, T8787-50ML) in PBS for 2 min. Next, cells were washed with PBS and fixed with 4 % PFA in PBS for 15 min. Following fixation, cells were washed with PBS wash, permeabilized with 0.2 % Triton-X in PBS for 4 min and washed with PBS again. For EdU staining, Click-iT reaction solution (100 mM Tris-HCl pH 8.5, 1 mM $CuSO_4$, 100 mM ascorbic acid, 0.9 μg Alexa Fluor 594 Azide [Invitrogen, A10270]) was added, and cells were incubated in the dark for 30 min. Cells were then blocked in 5 % BSA in PBS for 45 min, followed by application of primary antibodies against ATR (1:300, Cell Signaling Technology, 13934) and RNAPII (1:2000, Merck Millipore, 05-623), CDK1 (1:500, Novus Biologicals, NBP2-37626) and MED1 (1:200, Cell Signaling Technology, 551613S), or CDK2 (1:200, Millapore Sigma, AMAB91497) and MED1 (1:200, Cell Signaling Technology, 551613S) diluted in 5 % BSA in PBS. Cells were incubated at 4°C overnight. The next day, cells were washed twice with PBS. Subsequently, Duolink PLUS (Millipore Sigma, DUO92001) and MINUS (Millipore Sigma, DUO92005) probes diluted with Duolink Antibody Diluent (1:10) were applied for 1 h at 37°C. The cells were washed twice with Wash buffer A (Millipore Sigma, DUO82049) and the ligation solution (1x Duolink ligation buffer, Ligase at

1:70 dilution; Millipore Sigma, DUO92014) was applied for 30 min at 37°C. After two additional washes with Wash buffer A the amplification solution (1x Amplification buffer, Polymerase at 1:140 dilution; Millipore Sigma, DUO92014) was added and cells were incubated in the dark at 37°C for 100 min. The cells were then washed twice with Wash buffer B (Millipore Sigma, DUO82049) and stained with DAPI in 3 % BSA in PBS for 1 h. Finally, cells were washed twice with PBS and stored at 4°C until imaging. Images were acquired on a Nikon T2 inverted microscope equipped with an Andor Dragonfly spinning disk, a 40X air objective, and an iXon Life 888 EMCCD camera. Per condition 81 positions were imaged at which a Z-stack of 7 images across 10 μm was acquired. Image analysis was conducted in ImageJ Fiji[49] as described previously.[51] Specifically, a single focal plane image was extracted based on the highest fluorescence variance plane and the background was subtracted using the modal pixel intensity value as the background. Segmentation of nuclei was performed using Fiji's built-in thresholding on the nuclear stain. Fluorescence intensity of the EdU labeled channel was measured to identify the S phase population, and PLA foci were quantified using the Fiji Maxima Finder tool.

ATR CUT&RUN and 4sU-seq data visualization

Previously published 4sU-seq and CUT&RUN data[21] were visualized using deepTools (v3.5.1).[52] The data were centered at the transcription start site for all protein-coding genes excluding chrX, Y, and mitochondrial genes. The 55 histone genes are located on chr6 within the 25.7Mb-27.9Mb using hg19 gene annotations. Negative control regions were randomly selected 2Mb regions with 55 protein-coding genes, excluding the histone gene cluster on chr6. Additional negative controls were random 55 genes and 55 single-exon genes, and the median enrichment of signals across multiple iterations (n=22) were plotted using deepTools plotHeatmap.

CRISPR screen reanalysis

The genome-wide CRISPR knockout screening data was obtained from Wang et al.[35] The normalized Z-scores were averaged across the cell lines and plotted using R (v4.3.3) with ggrepel (v0.9.6) and ggside (0.3.1).

RNA fluorescence in situ hybridization (RNA-FISH)

Cells were grown in 96-well plates with a glass-like polymer well-bottom (Cellvis P96-1.5P) and treated with inhibitors (AZD6738 (5 μM), LY2603618 (2 μM), or aphidicolin (1 μM) for 4 hours. S phase cells were labeled with EdU for 15 minutes prior to fixation. Cells were fixed, permeabilized, and H1.1 RNA was labeled using the ViewRNA Cell Plus Assay kit (Thermo Fisher Scientific, 88-19000). H1.1 RNA was detected using probes (Thermo Fisher Scientific, Viewrna Cell Plus Probe Set, Alexa Fluor 488, HIST1H1A, VA4-3086709-VCP). Labeling was done following manufacturer's recommendation. After imaging RNA-FISH signals, cells were washed with 3% BSA/PBS and incubated with the Click-iT reaction mixture with 1 μg/ml of Alexa Fluor™ 647 Azide for 30 min with at room temperature on a bench rocker. After the Click-iT reaction, cells were washed with 3% BSA/PBS, followed by washed 3 times in 1X PBS, and then the EdU signal was imaged at the same field of view as RNA-FISH images. Total H1.1 RNA foci (nuclear and cytoplasmic) were counted using Cellprofiler and S phase cells were detected by EdU signal.

Plasmid transfection

MCF10A cells were seeded at 8,000 cells per well 96-well plates with a glass-like polymer well-bottom (Cellvis P96-1.5P). 24 h post-seeding, cells were transfected with pEGFP-H1.1 plasmid (Addgene, 32894) using FuGENE® 6 transfection reagent (Promega, E2691), following manufacturer's guidelines. A transfection mixture was prepared by first adding FuGENE® 6 transfection reagent to Opti-MEM medium, followed by the addition of DNA at a ratio of 3:1 FuGENE® 6 transfection reagent to DNA. The mixture was incubated for 15 minutes at room temperature. For each well, 0.6 μL of FuGENE® 6 transfection reagent, 0.2 μg of DNA, and 10 μL of Opti-MEM medium were used. The transfection mixture was then added directly to the existing media in each well. The medium containing the transfection mixture was replaced with fresh medium 24 h post transfection. Cells were analyzed 48 h post-transfection.

Construction and expression of mNeonGreen-MED1^{IDR} WT and mutant in MCF10A cells

The MED1^{IDR} vectors were constructed by incorporating MED1^{IDR} WT or mutant into a core plasmid, LTO-NG. The LTO-NG plasmid has a lentivirus transfer vector backbone with a doxycycline-inducible promoter (TetON) regulating the expression of the mNeonGreen reporter protein. Additionally, it includes a SV40 promoter controlling the expression of rtTA3, which is linked to the blasticidin-resistant marker via a 2A peptide cleavage sequence. The lentivirus transfer vector backbone was derived from the pCW57.1 plasmid (Addgene, 41393), while the mNeonGreen gene originated from the mNeonGreen-mTurquoise2 plasmid (Addgene, 98886). The rtTA3 gene, fused to the blasticidin-resistant marker (BlastR), was adapted from the pLenti CMV rtTA3 Blast (w756-1) plasmid (Addgene, 26429). The MED1^{IDR} WT and mutant DNA sequence were synthesized as 5 smaller sequence blocks, each containing a singular phospho-domain. These phospho-domains were engineered to express in either an 'ON' state, wherein all serine/threonine (S/T) residues known to undergo phosphorylation within the domain were substituted with aspartic acid (D), or an 'OFF' state, where these residues were replaced with alanine (A). The sequence blocks were synthesized along with its associated phospho-domain in the desired 'ON' or 'OFF' state, with flanking BsmBI sites enabling scarless fusion between blocks, using Integrated DNA Technologies g-Block service (https://www.idtdna.com/). Subsequently, these sequence blocks were integrated into the LTO-NG plasmid in desired combinations utilizing BsmBI-mediated Golden Gate cloning. The resultant vectors expressed MED1^{IDR} WT or mutant fused to the C-terminus of the mNeonGreen reporter. This vector was utilized to produce lentivirus and transduced MCF10A cells, as detailed below. Transduced cells underwent selection for positive vector integration by culturing in media supplemented

with 10 μg/ml of blasticidin (Invivogen, ant-bl-1) for a duration of 2 weeks, afterwards cells were considered stable cells integrated with the desired vector. For experimental procedures, stable cells were seeded in 96-well plates with a glass-like polymer well-bottom (Cellvis P96-1.5P) and subjected to treatment with 0.5 μg/ml doxycycline (Millipore Sigma, D5207-5G) for 24 h prior to live-cell imaging. Live-cell imaging was performed using a fully automated ImageXpress Micro system (Molecular Devices) at 40X magnification. During imaging, cells were maintained at 37°C in an atmosphere with 5% CO2. Image analysis was performed using quantitative image-based cytometry analysis, as described above.

Lentivirus production and transductions

Second generation lentiviruses were generated using HEK-293T cells. Cells were transfected using FuGENE® 6 transfection reagent (Promega, E2691) in a 100 mm tissue culture dish format per transfer vector. Briefly, a transfection mixture was prepared by diluting 6 μg of the transfer vector (i.e., mNeonGreen-MED1^{IDR} variant vectors), 6 μg of the psPAX2 plasmid (Addgene plasmid no. 12260) and 0.6 μg of the pMD2.g plasmid (Addgene, 12259) in Opti-MEM medium (Thermo Fisher Scientific, 31985062) and mixing with 36 μl FuGENE® 6 transfection reagent (Promega, E2691) according to the manufacturer's instructions. The transfection mixture was then added directly into a 100 mm tissue culture dish, followed by seeding 1x10^{6} cells and a gentle swirling to ensure uniform distribution. The medium was replaced with fresh medium 8 h post transfection and the virus-containing medium was collected after 48 h. The virus was concentrated using the Lenti-X concentrator (Clontech, 631232) according to the manufacturer's protocol. Cell transduction was performed by seeding MCF10A cells onto 12-well tissue culture plates at a density of 1x10^{5} cells per well. After 24 h, the medium was replaced with medium containing 2X concentrated virus medium and 8 μg/ml polybrene (Millipore Sigma, TR-1003-G). The virus-containing medium was replaced with medium supplemented with 24 h post transduction.

Analysis of MED1^{IDR} phosphorylation state in S phase cells

Analysis of phosphorylation events on MED1^{IDR} (560 - 1582 aa) was performed by clustering observed phosphorylation sites[37] within the MED1^{IDR} into phospho-domains (PDs). These PDs were demarcated by i) the cell cycle stage information associated with the phosphorylation sites and ii) the proximity of these phosphorylation sites (Table S1). Heatmap values showing phosphorylation state in Figure S7F were calculated by summing the Ratio H/M Normalized Log2 values of each phospho-site within the given phospho-domain.

QUANTIFICATION AND STATISTICAL ANALYSIS

Statistical metrics encompassing the number of biological replicates (n), standard deviation and statistical significance are reported in both the visuals graphs and the accompanying figure captions. The threshold for determining statistical significance has been established at a p-value less than 0.05, assessed using two-tailed Student's t-test or One-Way ANOVA test, contingent on the specific requirements of the data set under evaluation.